The Astrophysical Journal, 823:130 (15pp), 2016 June 1 doi:10.3847/0004-637X/823/2/130

SUB-INERTIAL GRAVITY MODES IN THE B8V STAR KIC 7760680 REVEAL MODERATE CORE OVERSHOOTING AND LOW VERTICAL DIFFUSIVE MIXING

Ehsan Moravveji[1,5], Richard H. D. Townsend[2], Conny Aerts[1,3], and Stéphane Mathis[4]
[1] Institute of Astronomy, KU Leuven, Celestijnenlaan 200D, B-3001 Leuven, Belgium; Ehsan.Moravveji@ster.kuleuven.be
[2] Department of Astronomy, University of Wisconsin-Madison, Madison, WI 53706, USA
[3] Department of Astrophysics, IMAPP, Radboud University Nijmegen, P.O. Box 9010, 6500 GL, Nijmegen, The Netherlands
[4] Laboratoire AIM Paris-Saclay, CEA/DSM—CNRS—Université Paris Diderot, IRFU/SAp Centre de Saclay, F-91191, Gif-sur-Yvette Cedex, France
Received 2016 March 25; accepted 2016 April 1; published 2016 May 31

ABSTRACT

Thus far, KIC 7760680 is the richest slowly pulsating B star, exhibiting 36 consecutive dipole ($\ell = 1$) gravity (g-) modes. The monotonically decreasing period spacing of the series, in addition to the local dips in the pattern, confirm that KIC 7760680 is a moderate rotator with clear mode trapping in chemically inhomogeneous layers. We employ the traditional approximation of rotation to incorporate rotational effects on g-mode frequencies. Our detailed forward asteroseismic modeling of this g-mode series reveals that KIC 7760680 is a moderately rotating B star with mass $\sim 3.25\,M_{\odot}$. By simultaneously matching the slope of the period spacing and the number of modes in the observed frequency range, we deduce that the equatorial rotation frequency of KIC 7760680 is 0.4805 day^{-1}, which is 26% of its Roche break up frequency. The relative deviation of the model frequencies and those observed is less than 1%. We succeed in tightly constraining the exponentially decaying convective core overshooting parameter to $f_{\rm ov} \approx 0.024 \pm 0.001$. This means that convective core overshooting can coexist with moderate rotation. Moreover, models with exponentially decaying overshoot from the core outperform those with the classical step-function overshoot. The best value for extra diffusive mixing in the radiatively stable envelope is confined to $\log D_{\rm ext} \approx 0.75 \pm 0.25$ (with $D_{\rm ext}$ in cm^2 s^{-1}), which is notably smaller than theoretical predictions.

Key words: asteroseismology – diffusion – stars: individual (KIC 7760680) – stars: interiors – stars: rotation – waves

1. INTRODUCTION

Late- to mid-type B stars have masses between ~3 and 7 $M_{\odot}$, and are pulsationally unstable against low-degree, high-order $|n_{\rm pg}| \gtrsim 10$ g-modes, with periods ranging from ~0.5 to ~3 days. They are classified as slowly pulsating B (SPB) stars (Waelkens 1991; Waelkens et al. 1998; De Cat & Aerts 2002; Aerts et al. 2010). Non-adiabatic heat exchange around the iron opacity bump at $\log T \approx 5.2$ K—known as the classical κ-mechanism—is responsible for their mode excitation (Dziembowski et al. 1993; Gautschy & Saio 1993). Together with γ Dor stars, they are the richest main-sequence g-mode pulsators with numerous excited modes (e.g., Figure 2(e) in Moravveji 2016). Chemically inhomogeneous regions above the receding convective cores reside inside this propagation cavity, and allow for partial or complete g-mode trapping, providing a unique physical diagnostic of the chemical mixing and thermal stratification in the deep stellar interior (Miglio et al. 2008; Cunha et al. 2015). In addition, g-modes can have sizeable amplitudes inside the narrow overshooting region—between the fully mixed convective core and the μ-gradient layer, allowing us to constrain the extent and physical properties of the overshooting layer (Dziembowski & Pamyatnykh 1991; Moravveji 2015; Moravveji et al. 2015). In such circumstances, g-modes can resolve and probe the physical conditions of the overshooting layer.

Moderate to rapid rotation is a fairly well-established property of (single and binary) SPB stars (Huang et al. 2010), and in general massive stars (Dufton et al. 2013; Ramírez-Agudelo et al. 2013, 2015). As soon as rotation kicks in, the centrifugal force deforms the star, and large-scale advection sets in. Then, the thermal and structural equilibrium of stars undergo a readjustment in order to conserve mass, energy, and linear and angular momentum (Kippenhahn & Thomas 1970; Endal & Sofia 1976, 1978; Zahn 1992; Maeder & Zahn 1998; Mathis & Zahn 2004; Maeder 2009; Espinosa Lara & Rieutord 2013). As a consequence of this, a handful of (advective and diffusive) mixing processes are triggered, smoothing chemical inhomogeneities in the radiative envelopes and transferring angular momentum between the stellar core and envelope (see, e.g., Endal & Sofia 1978; Heger et al. 2000, 2005; Maeder 2009). This poorly known aspect of the theory of stellar evolution deserves a profound observational calibration. From the observational and theoretical standpoints, however, there is a long road ahead to test and grasp all of the proposed mixing mechanisms and the possible interplay between them (Heger et al. 2000; Maeder et al. 2013). Using the asteroseismology of rotating and heat-driven pulsating stars, such as SPBs and γ Dor stars, we can quantitatively address several uncertain aspects of massive star evolution and deep internal structure. The very slowly rotating pulsating *Kepler* B8V star KIC 10526294 (Pápics et al. 2014, hereafter Star I) offered the first opportunity for seismic modeling of this type of pulsator. In Moravveji et al. (2015), we succeeded in placing tight asteroseismic constraints on core overshooting and extra diffusive mixing in the envelope of this star. That was followed by the derivation of its internal differential rotation profile by Triana et al. (2015), who inferred that the envelope of Star I rotates in the opposite direction with respect to its core.

Pulsation instability among late B-type stars is a known phenomenon from ground-based photometric and spectroscopic observations (De Cat & Aerts 2002), as well as from

[5] Marie Curie post-doctoral Fellow.

CoRoT and *Kepler* space photometry (Balona et al. 2011; Pápics et al. 2011, 2012). The impact of rotation on pulsation modes is profound, and has been thoroughly explained in the literature. For instance, Unno et al. (1989) and Townsend (2003a) explain the different classes of heat-driven inertial pulsation modes that arise in rotating stars, such as Rossby (r-) modes, Kelvin modes, and Yanai modes, because of the action of the Coriolis acceleration. The centrifugal deformation of the star affects the low-density outer envelope more significantly than the high-density core; thus, p-modes are more influenced by the centrifugal force, while g-modes are influenced by the Coriolis force (Dintrans & Rieutord 2000; Reese et al. 2006; Ballot et al. 2010). In addition to heat-driven modes destabilized by rotation, stochastic excitation of gravito-inertial waves was predicted by Mathis et al. (2014) and Rogers et al. (2013), and observed by Neiner et al. (2012) in the *CoRoT* B0IVe target HD 51452. The feedback from low-frequency g-modes and r-modes in SPB stars is the efficient transport of angular momentum (Lee et al. 2014, 2016; Rogers 2015). Nonradial pulsations are even proposed to cause the Be phenomena through the energy leakage of low-frequency, prograde g-modes (Shibahashi & Ishimatsu 2013). This was already observed in B0.5IVe *CoRoT* target HD 49330 (Huat et al. 2009). Thus, rotation interacts profoundly with stellar structure, evolution, and pulsation.

The pulsation description of rotating stars is at least a two-dimensional problem (e.g., Prat et al. 2016). However, it is possible to reduce this dimensionality into two separate one-dimensional (1D) problems for the radial (Lee & Saio 1986) and angular dependence (Lee & Saio 1997; Townsend 2003b) of eigensolutions. This is achieved by ignoring the centrifugal deformation and neglecting the horizontal component of the rotation vector in the momentum equation when stratification dominates rotation (see, e.g., the detailed discussion in Mathis et al. 2008). This is historically known as the Traditional Approximation of Rotation (TAR; Eckart 1960). Within the TAR framework, Townsend (2005a, 2005b) and Aprilia et al. (2011) have shown that the combination of buoyancy and Coriolis forces, when coupled with the κ-mechanism due to the iron bump, provide a sufficient restoring force for driving high-order prograde $m = +1$ g-modes in SPB and γ Dor stars (Savonije 2005; Bouabid et al. 2013). In addition, these modes are predicted to exhibit significant photometric light variability and to become observable (Townsend 2003a; Savonije 2013).

The theoretical basis and observational facilities are now in place to exploit the wealth of information contained in the frequency spectrum of rotating, pulsating B stars. The subject of this paper is the modeling and initial interpretation of a moderately rotating and slowly pulsating B8V star KIC 7760680 that was recently discovered by Pápics et al. (2015). We employ the identified series of dipole prograde g-modes in this star to address the following basic questions regarding the internal structure and global evolution of massive stars. (a) How can we constrain the unknown rotation frequency of a rotating SPB star? (b) Does rotation suppress core overshooting? (c) What are the combined and simultaneous effects of core overshoot mixing and additional mixing in the radiatively stable envelopes of B stars? (d) Does the efficiency of the overshooting mixing decline radially from the fully mixed convective core, or does it stay strongly efficient over a fraction of scale heights away from the core boundary? Here, we provide answers to this set of questions using a forward seismic modeling of our target star.

In Section 2, we introduce the seismic observables of KIC 7760680 which we exploit, and justify using a traditional approximation when modeling high-order g-modes. The treatment of overshooting and extra diffusive mixing in the radiative envelope is the subject of Section 3, which is then followed by the introduction of the input physics of four asteroseismic grids of non-rotating models in Section 4. The evolutionary models are computed with the 1D MESA stellar structure and evolution code (Paxton et al. 2011, 2013, 2015, version 7678). The TAR and a comparison with first-order frequency perturbation are presented in Section 5. Our asteroseismic computations are performed with the GYRE (version 4.2) linear nonradial adiabatic/non-adiabatic 1D pulsation code (Townsend & Teitler 2013) that incorporates TAR. We introduce a simple and robust scheme to optimize the unknown rotation frequency of the star in Section 6, and statistically constrain the most likely rotation rate of the target. The meric function that we use for model selection is discussed in Section 7. In Section 8, we proceed to choose the best asteroseismic model that reproduces the observed slanted period spacing pattern, and elaborate on mode stability properties and their efficient trapping in the overshooting region. In Section 9, we summarize our findings and discuss the missing input physics from current state-of-the-art 1D evolutionary models, which need to be incorporated in the (near) future.

2. ASTEROSEISMIC OBSERVABLES OF KIC 7760680

KIC 7760680 (B8 V) was observed by the nominal *Kepler* satellite for nearly four years. Pápics et al. (2015) carried out a thorough observational analysis of this target; below, we summarize their findings which are relevant to our modeling. The spectroscopic properties of KIC 7760680 from HERMES (Raskin et al. 2011) high-resolution spectra are $T_{\rm eff} = 11650 \pm 210$ K, $\log g = 3.97 \pm 0.08$ dex, $[M/H] = 0.14 \pm 0.09$, and $v \sin i = 62 \pm 5\,{\rm km\,s^{-1}}$. The inferred $T_{\rm eff}$ and $\log g$ place KIC 7760680 at the low-mass end of the SPB instability strip (Pamyatnykh 1999; Moravveji 2016).

Pápics et al. (2015) identified a series of $\mathcal{N} = 36$ low-frequency modes with periods between $P_1 \pm \sigma_1 = 0.86930 \pm 0.00002$ and $P_{36} \pm \sigma_{36} = 1.46046 \pm 0.00004$ days (their Table 1). This marks KIC 7760680 as the richest SPB discovered so far. Figure 1(a) shows the observed period spacing ΔP, and Figure 1(b) shows the relative frequency uncertainty $\sigma_i / f_i^{\rm (obs)}$ around each mode. The striking feature of this series is the contiguous period spacing pattern with a negative slope. In a non-rotating star, the asymptotic period spacing is $\Delta P_\ell^{\rm (asy)} = 2\pi^2 \left(\sqrt{\ell\,(\ell+1)} \int_{r_0}^{r_1} N / r\, dr \right)^{-1}$, with r_0 and r_1 being the inner and outer turning points of the mode propagation cavity, and the Brunt–Väisälä frequency N (Tassoul 1980). For a star with rotation frequency $f_{\rm rot}$ and pulsation g-mode frequency $f_i^{\rm (co)}$ in the co-rotating frame, the spin parameter is defined as $s_i = 2 f_{\rm rot} / f_i^{\rm (co)}$, and the period spacing $\Delta P_{\ell,m}^{\rm (co)}(s)$ is

$$\Delta P_{\tilde{\ell},m}^{\rm (co)}(s) \simeq \frac{2\pi^2}{\sqrt{\lambda_{\tilde{\ell},m,s(n+1)}} \int_{r_0}^{r_1} \frac{N}{r} dr \left(1 + \frac{1}{2} \frac{d \ln \lambda_{\tilde{\ell},m,s(n)}}{d \ln s} \right)}, \quad (1)$$

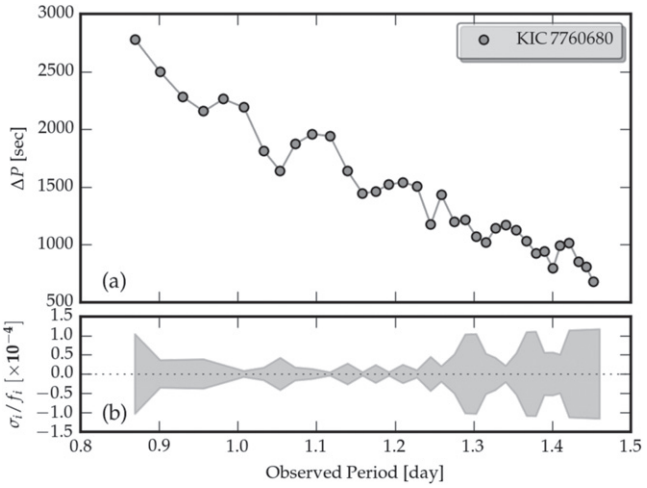

Figure 1. (a) The observed period spacing of KIC 7760680, consisting of 36 dipole prograde g-modes. For the list of observed modes, refer to Table 1 in Pápics et al. (2015). The uncertainties are smaller than the plotting symbols. (b) The observed relative frequency uncertainty $\sigma_i/f_i^{(\mathrm{obs})}$. Note that the ordinate is rescaled by a factor of 10^{-4} for better visibility. The modes in the middle of the series have the highest precision.

where $n, \tilde{\ell}, m$ are mode wavenumbers, and $\lambda_{\tilde{\ell},m,s}$ is the eigenvalue of the Laplace Tidal equation (Townsend 2003b; Ballot et al. 2012; Bouabid et al. 2013). For $f_{\mathrm{rot}} = 0$, $\lambda_{\tilde{\ell},m,s}$ reduces to $\ell(\ell+1)$. Based on Equation (1), period spacing depends sensitively on the thermal and chemical stratification through the Brunt–Väisälä frequency N, in addition to the star's rotation and pulsation frequencies through the spin parameter s. Thus, it provides a powerful asteroseismic diagnostic for constraining a star's internal structure, in addition to its rotation frequency. Here, we attempt to model the observed pulsation freqeuncies and reproduce the period spacing in Figure 1(a).

By a visual inspection of the observed period spacing pattern in Figure 1(a), two important inferences follow: (a) the negative moderate slope unravels the fact that KIC 7760680 is a moderate rotator. A comparison with Figure 4 in Bouabid et al. (2013) and Figures 4 and 5 in Van Reeth et al. (2015b) demonstrates that this series belongs to prograde modes, which are also theoretically predicted to be unstable in rotating SPB stars (Townsend 2005a, 2005b; Aprilia et al. 2011). (b) There are clear deviations from the (tilted) asymptotic period spacing, which manifest themselves as local dips. The reason behind this is the presence of an additional bump in the Brunt–Väisälä frequency, associated with the μ-gradient zone above the core (Miglio et al. 2008), giving rise to efficient mode trapping in this region (discussed in Section 8.3). This inference was shown earlier after a detailed asteroseismic modeling of Star I (Figure 2 in Moravveji 2015). This proves that the mixing in the radiative envelope is not strong enough to chemically homogenize the radiative zone. The presence of local dips in the observed period spacing puts an upper limit on the effective amount of chemical mixing in the radiative envelope of this rotating SPB.

The list of 36 dipole g-modes of KIC 7760680 was determined following the methodology discussed in detail in Degroote et al. (2009), which is based on the theory of time series analysis of correlated data (Schwarzenberg-Czerny 1991). Practically, we take the formal errors of the nonlinear least-squares fit to the light curve and correct them for the signal-to-noise ratio, sampling, and the correlated nature of the data. Based on this procedure, explained in Degroote et al., a correction factor of $Q = 4.0$ (P. I. Pápics 2016, private communication) is applied to the formal errors listed in Table 1 of Pápics et al. (2015).

For heat-driven pulsators, unambiguous mode identification from (*Kepler*) white-light photometry is only possible if one detects (almost) equally spaced frequency splittings around isolated peaks. Examples of such splittings can be found in Pápics et al. (2014), Kurtz et al. (2014), and Saio et al. (2015). While this was feasible for Star I, Pápics et al. (2015) could not discern any frequency splitting for KIC 7760680 due to the very high density of peaks in the narrow g-mode frequency domain. Thus, one cannot assume any harmonic degree ℓ and azimuthal order m for the detected series. To address this, we computed a few evolutionary tracks that pass through the 1σ position of the star on the Kiel diagram, and chose a model that closely reproduced the observed period spacing after including rigid rotation. Then, we computed period spacing patterns for all possible combinations of $1 \leqslant \ell \leqslant 2$ and $|m| \leqslant \ell$ to explain the detected spacing. Appendix A and Figure 11 present the results. The only possible way to simultaneously reproduce the slope of the observed series, the number of observed modes inside the observed range $\mathcal{N}$, and the location of the input model on the Kiel diagram (inside the 1σ spectroscopic box) is if the observed series is associated with dipole prograde (ℓ, m) = (1, +1) g-modes, which we adopt in the following.

3. A SIMPLIFIED MIXING SCHEME

Instead of exploiting non-exhaustive lists of proposed rotational and non-rotational mixing mechanisms (e.g., Heger et al. 2000, 2005; Maeder et al. 2013; Mathis 2013), we take a pragmatic approach and divide non-convective sources of mixing and their corresponding coefficients into two distinct categories: (a) overshooting from the convective core into the radiative interior in a diffusive regime D_{ov}, and (b) an effective extra diffusive mixing D_{ext} from the top of the overshoot layer up to the surface. Hereafter, D_{ext} is in $\mathrm{cm^2\,s^{-1}}$. Figure 2(a) depicts our adopted mixing scheme. In the core, convective mixing (blue) is computed from the Mixing Length Theory (MLT; Böhm-Vitense 1958; Cox & Giuli 1968); there, the temperature gradient is almost adiabatic $\nabla \simeq \nabla_{\mathrm{ad}}$. The overshoot region (gray) is installed at the outer boundary of the convective core. MLT does not apply in this region, and D_{ov} is instead calculated from an ad hoc prescription. In the present work, we consider two prescriptions offered by MESA.

A. Exponential overshoot (after Freytag et al. 1996; Herwig 2000) where the diffusion coefficient for overshoot has a radial dependence,

$$D_{\mathrm{ov}} = D_{\mathrm{conv}} \exp\left(-\frac{2(r-r_0)}{f_{\mathrm{ov}} H_p}\right) \qquad r_0 \leqslant r. \tag{2}$$

Here, $r_0 = r_{\mathrm{cc}} - f_0 H_p$ is the radial coordinate of the lower boundary of the overshoot region, which is situated at a depth $f_0 H_p$ below the radius r_{cc} of the convective core boundary; H_p is the pressure scale height, evaluated at r_{cc}; and D_{conv} is the convective mixing diffusion coefficient, evaluated from MLT at r_0. The dimensionless parameters f_0 and f_{ov} allow tuning of the position and exponential scale, respectively, of the overshoot region. We fix

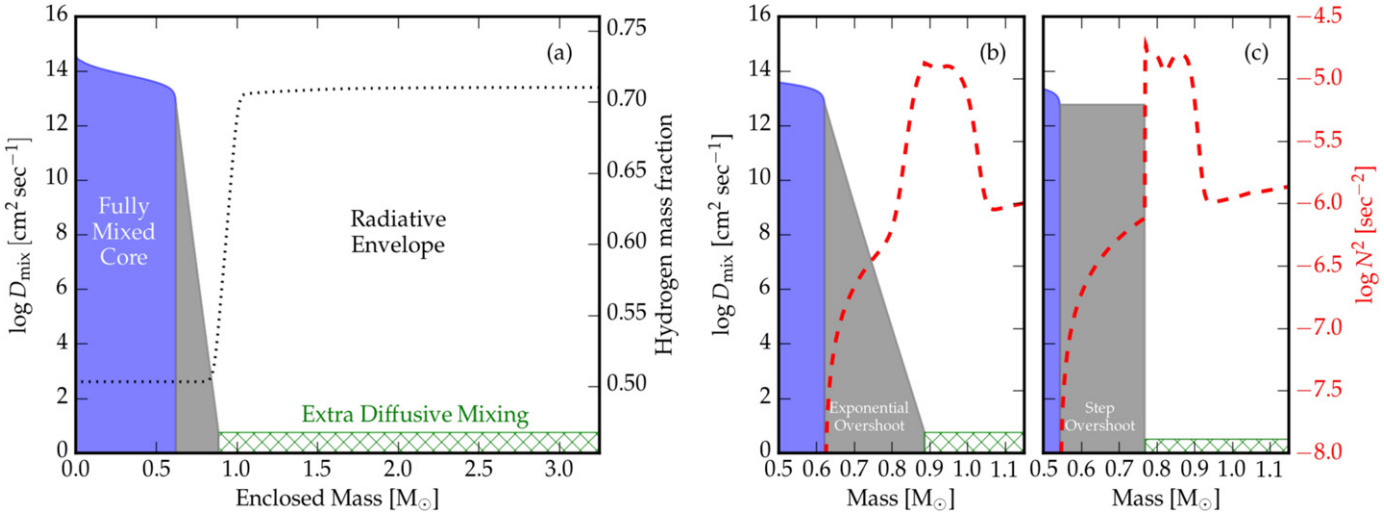

Figure 2. (a) The simplified mixing scheme in our evolutionary models, shown for the best asteroseismic model of KIC 7760680 (discussed in Section 8.1 and Table 2). The abscissa is the mass coordinate, and the ordinate is the logarithm of the mixing coefficient. The convective and overshooting regions are shown in blue and gray, respectively. Beyond the overshooting region, we include an additional diffusive mixing with varying strength (green hatch). The profile of the hydrogen mass fraction (dotted lines) shows that the overshoot region is fully mixed. (b) A zoom-in view around the overshoot region for the best model with an exponentially decaying prescription (Equation (2)). Grid A is built on this option. (c) Similarly, for the best model with step-function overshooting. Grid B is built on this option. Note the difference between the two Brunt–Väisälä profiles (red dashed line) and the extent of the two mixing regions.

$f_0 = 10^{-3}$ throughout the present work, but allow f_{ov} to vary.

B. Step overshoot, where the diffusion coefficient for overshoot has a fixed value,

$$D_{ov} = D_{conv} \qquad r_0 \leqslant r \leqslant r_0 + \alpha_{ov} H_p. \tag{3}$$

The interpretations of r_0, H_p, and D_{conv} are the same as before, and again we adopt $f_0 = 10^{-3}$ throughout; however, now the parameter α_{ov} tunes the extent of the overshooting zone.

In the overshoot region, MESA assumes $\nabla = \nabla_{rad}$; this differs from penetrative overshoot treatments (e.g., Roxburgh 1965; Maeder 1975; Zahn 1991; Viallet et al. 2015), which are similar to the step prescription B (above) but assume $\nabla = \nabla_{ad}$ over d_p, which is a penetration distance derived in Zahn (1991). The time-dependent turbulent convection model of Zhang (2016) allows us to set ∇ between ∇_{ad} and ∇_{rad}, but those models have not yet been confronted with observations.

In Figures 2(b) and (c), we present the exponentially decaying and step-function prescriptions, respectively. The two best seismic models of our target (discussed later in Section 8.1) are used as input. For the former, the transition from overshoot to extra mixing in the envelope is smooth. On the other hand, the step-function overshoot mixing, as in Figure 2(b), implies constant mixing inside the overshoot zone, and suddenly drops by ~13–7 orders of magnitude depending on what we adopt for D_{ext}. Here, the transition from overshoot to extra mixing is not smooth. The resulting Brunt–Väisälä frequencies N^2 are shown in both panels with red dashed lines. The difference between the two adopted overshoot prescriptions is that in the case of step-function overshoot, N^2 rises steeply at the top of the overshoot layer, whereas in the exponentially decaying model, N^2 grows smoothly. These two different N^2 profiles result in two different period spacing patterns, and allow us to discriminate between them when modeling SPB stars.

Finally, a constant extra diffusive mixing (green hatch) is applied above the overshoot region across the remaining part of the radiative envelope (with $\nabla = \nabla_{rad}$, see Figure 2). The extra mixing can be associated with advecto-diffusive mixing due to rotation instability (Heger et al. 2000; Maeder 2009), mixing by an internal magnetic field (Heger et al. 2005; Mathis & Zahn 2005), semi-convective mixing (Langer et al. 1985), internal gravity waves (Talon & Charbonnel 2005; Pantillon et al. 2007; Rogers et al. 2013; Rogers 2015), and other possible sources including their complex interaction (e.g., Maeder et al. 2013). Our proposed scheme is the least model-dependent approach to quantify the order of magnitude of the non-convective (diffusive) mixing coefficients beyond the fully mixed core in B stars.

Because both D_{ov} and D_{ext} are unconstrained from first principles, we parametrize them and scan the parameter space to find the optimal values that explain the observed pulsation frequencies (or equivalently period spacing) of our target. We recently developed this approach in Moravveji et al. (2015), and carried out a detailed forward modeling of 19 dipole ($\ell = 1$) g-modes in Star I (B8 V, $v \sin i < 18$ km s^{-1}). For this specific star, we found the diffusive exponential overshooting prescription more favorable than the step-function prescription, and confined the free overshooting parameter to $f_{ov} \approx 0.017$. Moreover, including extra diffusive mixing with a coefficient of $\log D_{ext} = 1.75$ improved the quality of the frequency fitting by a factor of ~11. This was the first asteroseismic quantification of extra mixing in B stars. Here, we apply the same methodology to KIC 7760680, which rotates much faster than Star I.

4. ASTEROSEISMIC MODELS

We compute non-rotating, non-magnetic stellar structure and evolution models with MESA with the mixing scheme described in Section 3. Each evolutionary track is specified with the following three parameters at the zero-age main sequence: the initial mass M_{ini}, core overshooting free

Table 1
Parameters of the Two Asteroseismic Grids for KIC 7760680

Grid	From	To	Step	N
A				
$M_{\rm ini}$ ($M_\odot$)	3.00	3.60	0.05	13
$f_{\rm ov}$	0.007	0.031	$\geqslant$0.001	13
$Z_{\rm ini}$	0.014	0.023	$\geqslant$0.001	8
$\log D_{\rm ext}$	None	5.0	$\geqslant$0.25	13
X_c	0.70	0.30	$\geqslant$0.001	$\sim$401
B				
$M_{\rm ini}$ ($M_\odot$)	3.00	3.40	0.05	9
$\alpha_{\rm ov}$	0.21	0.33	$\geqslant$0.01	9
$Z_{\rm ini}$	0.014	0.023	$\geqslant$0.001	4
$\log D_{\rm ext}$	None	1.50	$\geqslant$0.25	4
X_c	0.60	0.40	$\geqslant$0.001	$\sim$201

Note. We vary the initial mass $M_{\rm ini}$, exponential (or step-function) overshoot $f_{\rm ov}$ (or $\alpha_{\rm ov}$), initial metallicity $Z_{\rm ini}$, extra diffusive mixing $\log D_{\rm ext}$ (in cm^2 s^{-1}), and core hydrogen mass fraction (X_c). N is the total number of values for each parameter. The number of degrees of freedom for all grids is $n = 5$. "Step" gives the minimum step size in the corresponding parameter.

parameter $f_{\rm ov}$ (for exponential overshoot) or $\alpha_{\rm ov}$ (for step-function overshoot), and extra diffusive mixing beyond the overshoot region $D_{\rm ext}$. All of the models assume the Asplund et al. (2009) metal mixture with the initial hydrogen mass fraction $X_{\rm ini} = 0.71$ taken from the Galactic B-star standard of Nieva & Przybilla (2012). We vary the initial metallicity $Z_{\rm ini} \in [0.014, 0.023]$; the initial helium abundance is then fixed accordingly $Y_{\rm ini} = 1 - X_{\rm ini} - Z_{\rm ini}$. Along every evolutionary track, we store an equilibrium model at every $\sim$0.001 drop in X_c. We terminate the evolution as soon as X_c drops below 10^{-3}. The convective boundaries are specified using the Ledoux criterion. For the surface boundary condition, we use the ATLAS 9 tables of Castelli & Kurucz (2003) with surface optical depth $\tau_s = 2/3$. We include the line-driven mass loss prescription of Vink et al. (2001) with the efficiency factor reduced by a factor of 3 (Puls et al. 2015).

Recently, Moravveji (2016) showed that a 75% increase in the Iron and Nickel monochromatic opacities explains the position of two confirmed β Cep and eight confirmed hybrids on the Kiel diagram, which could not be explained before. The increase resulted from the direct laboratory Iron opacity measurement of Bailey et al. (2015), which was later confirmed by the numerical simulations of Nagayama et al. (2016). We use this set of OP Iron- and Nickel-enhanced opacity tables because it solves the pulsation instability problem in massive stars, in agreement with previous predictions (Dziembowski & Pamyatnykh 2008; Salmon et al. 2012). The recent OPAS opacity computation of Mondet et al. (2015) independently shows that the iron opacity is underestimated in default OP (Badnell et al. 2005; Seaton 2005) tables by $\sim$40% (their discussion in Section 5). Our computations are based on a 75% Fe and Ni enhanced opacity tables. The MESA lists and the opacity tables are freely available for download. More information is provided in Appendix B.

Based on the above setup, we compute two evolutionary grids with the range and stepsize of parameters listed in Table 1. The procedure is to start from a coarse parameter space, and iteratively zoom around the best parameter ranges by decreasing the parameter stepsize. The physical setups of both grids are identical, except for the choice of overshoot prescription. The exponential prescription is employed in grid A, where we vary $f_{\rm ov}$ (see Figure 2(b)); similarly, the step-function prescription is used in grid B, where we vary $\alpha_{\rm ov}$ (see Figure 2(c)). This allows us to assess which of the two overshooting prescriptions is superior, in the sense of providing a better fit to the observed frequencies. For Star I, we demonstrated that the exponential prescription outperformed the step-function one (Moravveji et al. 2015).

Extra diffusive mixing is one of the grid parameters that we vary from $\log D_{\rm ext} = 0.25$ to 5.0. We also include models suppressing this; these are presented in Table 1 and the forthcoming figures with "None." With this choice, we can examine if extra diffusive mixing is required in the envelope of SPB stars. For Star I, the χ^2 scores were reduced by a factor of more than 11 when we included extra mixing. Here, we re-examine this for KIC 7760680.

5. TRADITIONAL APPROXIMATION VERSUS FIRST-ORDER PERTURBATIONS

There are two possible approaches to incorporate the effect of rotation on pulsation frequencies based on 1D stellar models: one is through first-, second-, and third-order perturbative methods (Ledoux 1951; Dziembowski & Goode 1992; Soufi et al. 1998), and the other is through TAR. To assess the validity of the first-order perturbative approach (Ledoux 1951) versus TAR, one should consider the spin parameter s. Ballot et al. (2010) showed that for p-modes and low-order g-modes, it is still possible to use first-, second-, and/or third-order frequency corrections to reproduce the results from TAR for low values of the spin parameter $s \ll 1$ (refer to Bouabid et al. 2013, for γ Dor stars). As soon as $s_i \gtrsim 1$, the frequency splittings from perturbative methods depart from their counterparts within the TAR framework due to ignoring the impact of the Coriolis force on pulsation frequencies. This is the case for high-order g-modes—even in slowly rotating stars—due to their small frequency values.

To demonstrate this, Figure 3(a) compares the periods of dipole prograde modes from the first-order perturbative method (open circles) versus those from TAR (red dots) in the observer (inertial) reference frame. The spin parameter for the corresponding modes in the co-rotating frame is shown in Figure 3(b). The input model corresponds to the best asteroseismic model of KIC 7760680 (to be discussed later in Section 8), and is set to rotate rigidly at 26.4% of the Roche break up frequency. The range of the observed modes is shown by the blue band. The difference between the two sets of periods is considerable, and the resulting period spacing—which is tangent to each of these curves—will significantly differ. For sub-inertial waves, the wave dynamics is modified compared to TAR computations (Mathis et al. 2008, 2014); however, Ballot et al. (2012) have shown that the resulting period spacing within TAR gives a correct prediction up to high spin parameters. Consequently, even for sub-inertial g-modes $s > 1$, we decided to employ TAR.

Even though the centrifugal force implies deviations from spherical symmetry, this effect becomes important for stars rotating at more than half critical (Figure 1 in Aerts et al. 2004). Using Equations (1) and (2) in Aerts et al. (2004), the polar radius of our target is smaller than its equatorial radius by only $\sim$1.6%, when the star is set to rotate at 26% Roche critical

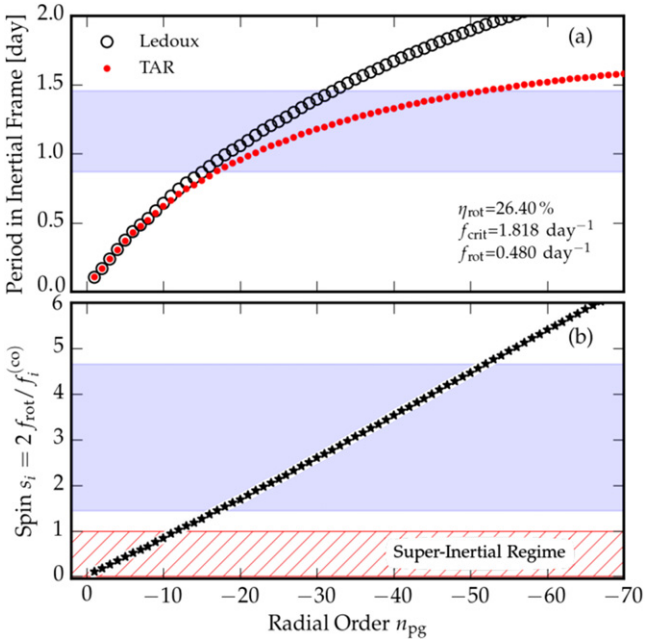

Figure 3. Top. First-order perturbative periods (empty circles) vs. those computed within TAR (red dots) in the inertial frame. The blue band highlights the observed period range of KIC 7760680. The equilibrium structure of the model is adapted to the best asteroseismic model of KIC 7760680 (Section 8), and is set to rotate rigidly at 26.4% of the Roche critical frequency. Bottom. The spin parameter for the corresponding mode frequencies in the co-rotating frame, $f_i^{\rm (co)}$. The observed modes (in blue band) fall outside the super-inertial regime $s \leqslant 1$ (red hatch), and lie in the sub-inertial regime $s > 1$.

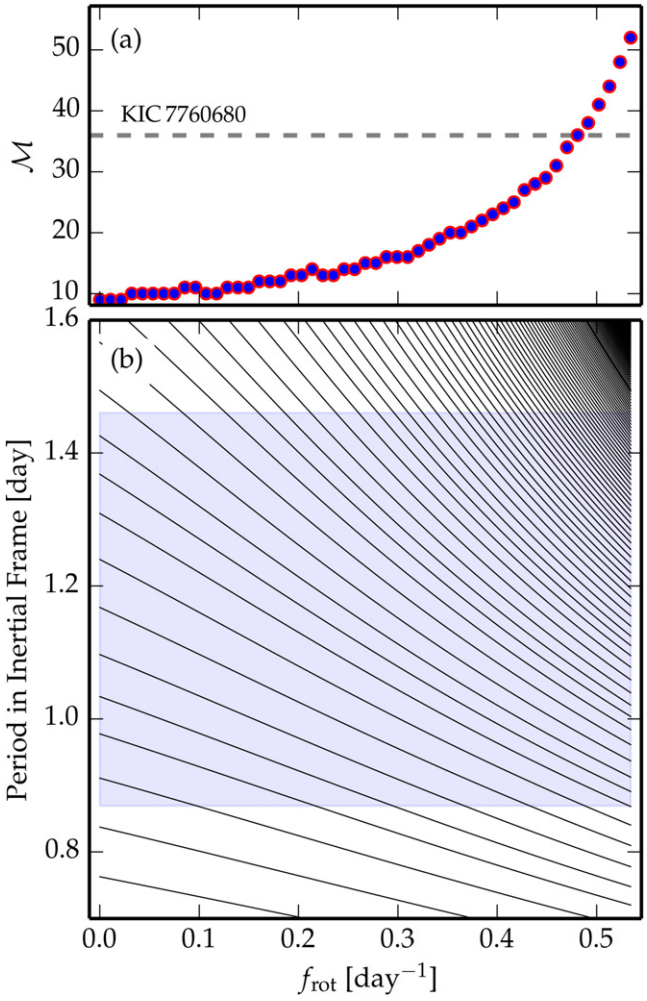

Figure 4. Top. The number of modes (circles) between the observed range (dashed line) $\mathcal{N}$ vs. rotation frequency $f_{\rm rot}$ in the inertial frame. Bottom. Evolution of the mode periods in the inertial frame $P_i^{\rm (in)}$ vs. $f_{\rm rot}$ for dipole prograde modes. We use the best model (Section 8.1 and Table 2) as input. The observed range $P_1 \leqslant P_i^{\rm (in)} \leqslant P_{36}$ is highlighted in blue. For higher $f_{\rm rot}$, a dense spectrum of high-order g-modes enters the observed range from the top, rapidly increasing $\mathcal{M}$.

frequency. Moreover, the stellar surface of slower rotators can deform significantly due to the effect of centrifugal force, and the deep interior—where high-order g-modes propagate with larger amplitudes—departs negligibly from spherical symmetry; see, e.g., Saio & Deupree (2012) for a demonstration. This means that modeling and studying the structure of the core overshooting layer in slow to moderate rotators with high-order g-modes using 1D stellar structure models coupled with 1D oscillation theory under TAR, and ignoring the centrifugal deformation, is fully justified.

6. OPMTIMIZING ROTATION FREQUENCY

The lack of prior knowledge on the inclination angle of the rotation axis of our target precludes deducing the equatorial rotation frequency $f_{\rm rot}$ from the spectroscopic measurement of the projected rotation velocity $v \sin i = 2\pi R_\star f_{\rm rot} \sin i = 62 \pm 5\,{\rm km\,s^{-1}}$, assuming a reasonable radius $R_\star$ from the models. Thus, $f_{\rm rot}$ is an additional unknown of KIC 7760680. Because MESA supports shellular rotation (Paxton et al. 2013), $f_{\rm rot}$ could be treated as another free parameter in our grids. However, we choose not to do so because, through their dependence on the spin parameter s_i, the g-mode frequencies are very sensitive to even a slight change in $f_{\rm rot}$ in the co-rotating and inertial frames. As a demonstration, see Figure 2 in Townsend (2005a) or Figures 1.1 and 2 in Bouabid et al. (2013). This would require an unreasonably broad and immensely resolved parameter survey for $f_{\rm rot}$, which is not computationally feasible. Instead, we take a pragmatic approach, and optimize $f_{\rm rot}$ for every input model. One can benefit from the observational fact that there are exactly $\mathcal{N} = 36$ observed modes between f_1 and f_{36} (allowing for a tolerance around them). Thanks to the high sensitivity of $\mathcal{N}$ to $f_{\rm rot}$, we can tune the latter until $\mathcal{N} = 36$ is satisfied.

Figure 4(b) shows the evolution of mode periods in the inertial frame versus the rotation frequency $f_{\rm rot}$. The blue band highlights the observed range. Clearly, increasing the rotation frequency (and hence the spin parameter) progressively increases the number of modes inside the observed range. At the same time, few modes gradually leave the observed range. The net number of modes inside the observed range $\mathcal{M}$ is shown in Figure 4(a), showing the strong dependence of $\mathcal{M}$ on $f_{\rm rot}$. The dashed horizontal line also shows the observed number of modes for KIC 7760680, i.e., $\mathcal{N} = 36$. We define $d\mathcal{N}(f_{\rm rot})$ as an integer-valued function that captures the difference between the model and observed number of modes in the inertial frame within the observed range:

$$d\mathcal{N}(f_{\rm rot}) = \mathcal{M} - \mathcal{N}. \quad (4)$$

Consequently, $d\mathcal{N}$ can be used as a discriminant to *optimize* the rotation frequency for every input model from our grids by

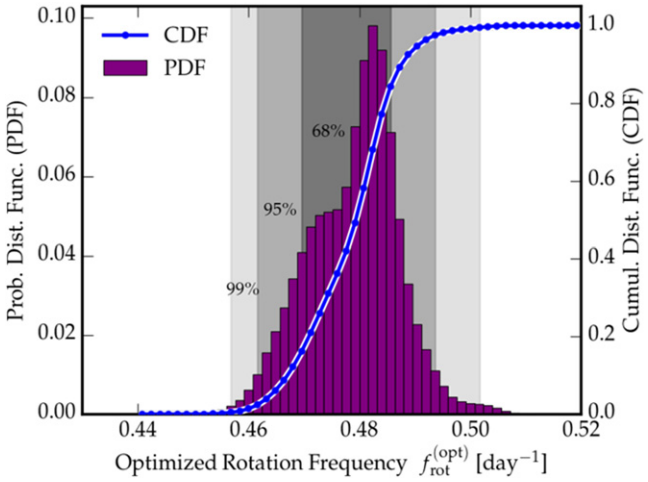

Figure 5. Histogram of the rotation frequency in grid A after rotation optimization $f_{\rm rot}^{\rm (opt)}$ (see Equation (5)). The blue curve is the cumulative distribution function (CDF) of the rotation frequency. The three shaded zones correspond to the rotation ranges where 99%, 95%, and 68% of $f_{\rm rot}^{\rm (opt)}$ lie, respectively.

seeking its root. Once the optimal rotation frequency $f_{\rm rot}^{\rm (opt)}$ is located, then

$$\mathcal{M} = \mathcal{N}, \quad \text{for} \quad f_{\rm rot} = f_{\rm rot}^{\rm (opt)}. \tag{5}$$

A brief description of the algorithm that locates the root of $d\mathcal{N}$ is given in Appendix C. Although we started from non-rotating models, we can optimize the rotation frequency assuming rigid rotation. Since our proposed algorithm has minimum underlying assumptions, we propose that it can be applied to any slow to moderately rotating star, including the *Kepler* sample of γ Dor stars of Van Reeth et al. (2015a, 2015b), provided that we limit the study to the prograde and/or zonal modes.

Figure 5 shows the histogram of the optimized rotation frequency for all models in grid A, which can be interpreted as the probability distribution function (PDF) of $f_{\rm rot}$ by requiring all of the models to fulfil Equation (5). The PDF exhibits a skewed distribution, strongly deviating from a Gaussian distribution. The striking result of our optimization scheme—reflected in the PDF—is that the $f_{\rm rot}^{\rm (opt)}$ for 99% of the models lies between 0.4568 and 0.5016 day^{-1}, which is already a tight constraint on the possible rotation frequency of the target. Similarly, 68% of rotation frequencies lie between 0.4696 and 0.4856 day^{-1}. The mean optimized rotation frequency $\langle f_{\rm rot}\rangle$ is simply a weighted average of the optimized rotation frequencies $f_{{\rm rot},k}^{\rm (opt)}$ within each histogram bin k, with the PDF within the same bin used as the weight w_k. In other words,

$$\langle f_{\rm rot}\rangle = \frac{\sum_k w_k f_{{\rm rot},k}^{\rm (opt)}}{\sum_k w_k}. \tag{6}$$

Together with the 1σ PDF range, the mean optimized rotation frequency of KIC 7760680 is $\langle f_{\rm rot}\rangle = 0.4790^{+0.0066}_{-0.0094}$ day^{-1}.

At the end of this step, we append $f_{\rm rot}^{\rm (opt)}$ to every model in our grids, ensuring that they reproduce the slope of the observed period spacing, and fulfil Equation (4). Now, we can proceed to compute the χ^2 goodness-of-fit scores (next section) to rank all of our input models accordingly.

7. MODEL FREQUENCIES AND RANKING

Each equilibrium structure model from our grids is fed into the adiabatic linear nonradial pulsation code GYRE using TAR. We compute dipole prograde frequencies within a broad trial range that ensures coverage of the observed period range. In GYRE, the frequencies are internally computed in the co-rotating frame, $f_i^{\rm (co)}$, for a trial rotation frequency, $\omega_{\rm rot} = 2\pi f_{\rm rot}$, but are stored in the inertial frame, $f_i^{\rm (in)}$, considering the Doppler shift, $f_i^{\rm (in)} = f_i^{\rm (co)} + m f_{\rm rot}$. This facilitates consistent comparison between the frequecies, periods, and/or period spacings from observations and models.

Because we optimize the rotation frequency (Section 6), we can proceed to a mode-by-mode comparison between observations and models. To rank all of the models based on their quality of fit to the observed frequencies (Table 1 of Pápics et al. 2015), we define a frequentist reduced-χ^2 score, denoted by $\chi^2_{\rm red}$:

$$\chi^2_{\rm red} = \frac{1}{\mathcal{N}-n}\sum_{i=1}^{\mathcal{N}}\left(\frac{f_i^{\rm (obs)} - f_i^{\rm (mod)}}{\sigma_i}\right)^2. \tag{7}$$

Here, $\mathcal{N} = 36$ is the number of observed modes, $n = 5$ is the number of free parameters in each grid for the fixed input physics, and the σ_i are the 1σ uncertainties of the observed frequencies. Consequently, we sort and tabulate all of the input models based on their associated $\chi^2_{\rm red}$. Based on this, we pick the two best models, one from grid A and the other from grid B, with minimum $\chi^2_{\rm red}$ scores. The properties of these models are discussed in Section 8.

8. RESULTS

8.1. Best Asteroseismic Model Candidates

Panels (a)–(e) in Figure 6 show the distribution of the logarithm of $\chi^2_{\rm red}$ versus the free parameters of grid A. The ordinate is limited to the lowest $\chi^2_{\rm red}$ values, despite $\chi^2_{\rm red} \in [1808, 2.11\times10^8]$. The $\log\chi^2_{\rm red}$ shows significant minima for most of the grid parameters, allowing us to tightly constrain them. Our best asteroseismic model corresponds to the one that has the minimum $\chi^2_{\rm red}$ within each grid. In what follows, we refer to the best model from grid A as mA, and that of grid B as mB. The internal structure of model mA is freely available for download, as explained in Appendix B. Figures 2(b) and (c) depict the internal structures of these two best models. Table 2 gives an overview of the physical properties of mA and mB, which we elaborate on below.

The large $\chi^2_{\rm red}$ values in Figure 6 are a common situation when modeling heat-driven modes with such high-precision frequencies. In spite of that, the most plausible parameters of KIC 7760680 are the following. The initial mass is roughly $M_{\rm ini} = 3.25\,M_\odot$, which is identical to that of Star I. Thus, KIC 7760680 is a moderately rotating analog of Star I. There is a clear indication that $Z_{\rm ini} \approx 0.020$, which agrees with the spectroscopic estimate that $[M/H] = 0.14 \pm 0.09$. Thus, KIC 7760680 is a metal-rich dwarf. From Figure 6(e), the age is well-constrained to $X_c = 0.50$, implying that KIC 7760680 is still in its early main-sequence evolution. The best value for the exponential overshooting parameter is $f_{\rm ov} = 0.024$, although $f_{\rm ov} \in [0.022, 0.026]$ result in comparatively good fits to the

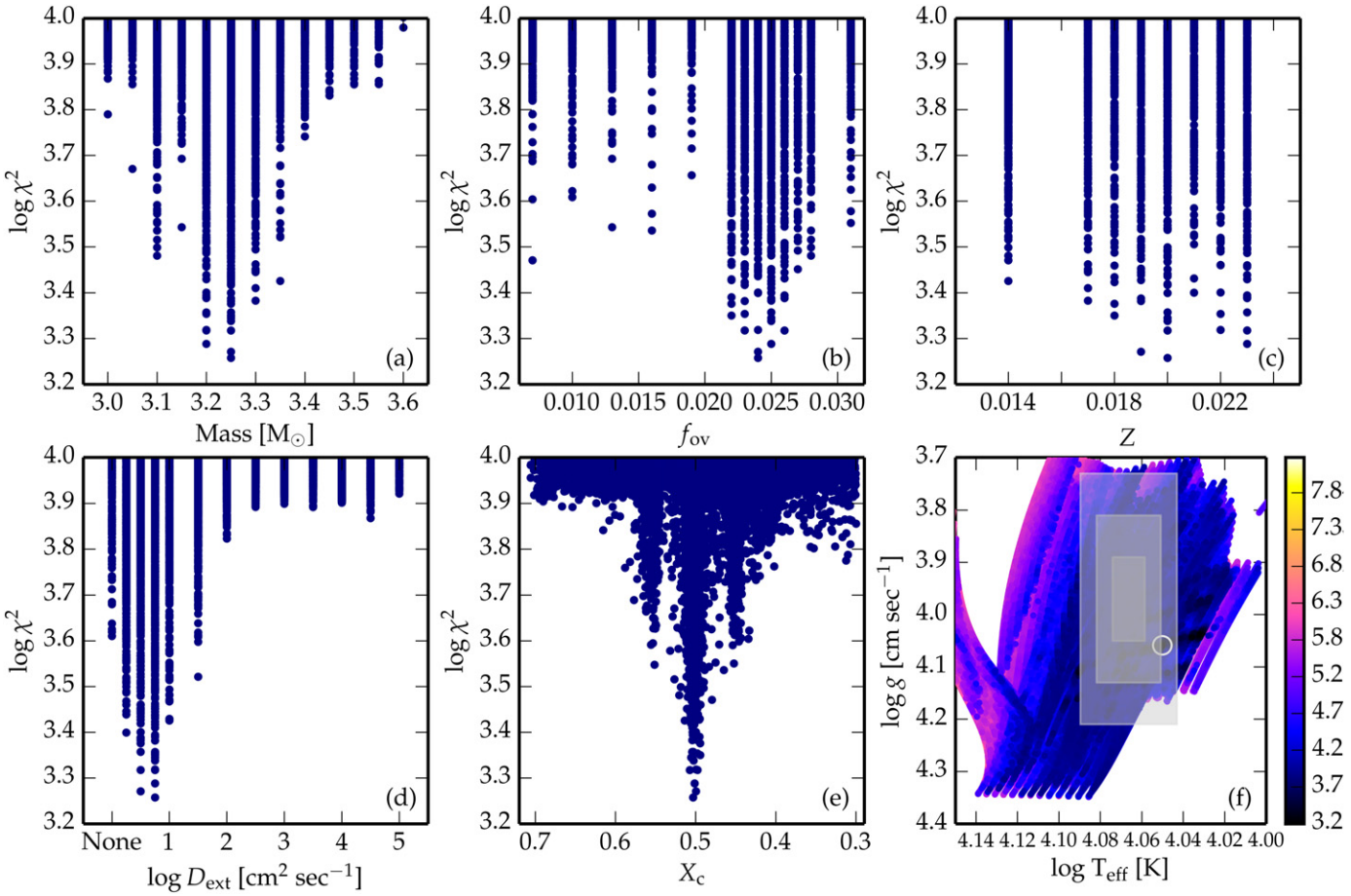

Figure 6. Distribution of $\log \chi^2_{\rm red}$ (Equation (7)) for the free parameters of grid A. A similar distribution for grid B is presented in Figure 7. Panels (a)–(e) show the local minima of $\log \chi^2_{\rm red}$ vs. initial mass $M_{\rm ini}$, exponential overshoot free parameter $f_{\rm ov}$, metallicity $Z_{\rm ini}$, extra diffusive mixing $\log D_{\rm ext}$, and center hydrogen mass fraction X_c, respectively. For clarity, the ordinate is restricted to models with $\log \chi^2_{\rm red} \leqslant 4$. Panel (f) shows the position of the input models on the Kiel diagram. The 1σ, 2σ, and 3σ uncertainty boxes for the position of KIC 7760680 from spectroscopy are highlighted as gray boxes. The position of the best model is flagged with a white open circle. The $\log \chi^2_{\rm red}$ is color-coded.

observed period spacing. Thus, the overshoot is stronger in this target compared to that of the slower rotator Star I.

The extra diffusive mixing exhibits a distinct minimum around $\log D_{\rm ext} \approx 0.75$. Theoretical predictions for the vertical (radial) component of the shear-induced mixing D_v in differentially rotating massive stars is roughly 3 to even 10 orders of magnitude stronger than what we constrained here; for several examples, refer to Figure 7 in Talon et al. (1997), Figure 6 in Meynet & Maeder (2000), Figure 3 in Mathis et al. (2004), and Figures 15 and 16 in Decressin et al. (2009). Based on Equation (7) in Mathis et al. (2004), D_v depends explicitly on the square of the angular differential rotation frequency $D_v \propto (r\, d\Omega/dr)^2$. The immediate—and perhaps most plausible—explanation of the low $D_{\rm ext}$ value is that KIC 7760680 is nearly a rigid-body rotator. The range of viable $D_{\rm ext}$ is so negligibly small that neglecting additional mixing in the radiative envelope is justifiable for this star. The extent of the three mixing regions, in addition to the profile of the hydrogen abundance and the Brunt–Väisälä frequency for the best model, are shown in Figure 2(a) and (b).

Figure 6(f) shows the position of all of the evolutionary tracks on the Kiel diagram. The color coding is proportional to $\log \chi^2_{\rm red}$. The 1σ, 2σ, and 3σ uncertainty boxes are highlighted in gray. The position of the best model is flagged with a white circle, which confirms that the asteroseismic parameters of the best model agree with their spectroscopic counterparts; recall that the same agreement was already achieved between $v \sin i$ and the optimized rotation frequency.

That the resulting $\chi^2_{\rm red}$ are larger than 1000 (even for the best models) stems from two facts. First, the relative uncertainties in the mode frequencies σ_i/f_i (see, e.g., Figure 1(b) or Table 1 in Pápics et al. 2015) are roughly $\sim 10^{-4}$–10^{-6}. Second, our current understanding of stellar structure and evolution is based on 1D models, imposing simplifying assumptions (e.g., stellar opacity, stellar composition and mixture, clumpiness in mass loss, treatment of rotation), ignoring some physical processes (e.g., atomic diffusion, radiative levitation, magnetic field), in addition to other physical processes that are not understood well (e.g., the role of internal gravity waves, the angular momentum transport, interaction of various mixing processes). Therefore, it is not surprising that our 1D equilibrium models succeed in explaining the overall asteroseismic observables globally, but not in detail.

The distribution of $\log \chi^2_{\rm red}$ for grid B (with step-function overshoot) is presented in Figure 7, and the grid parameters are given in Table 1. The $\log \chi^2_{\rm red}$ values lie in the range (3.562, 6.825). The preferred value for step-function overshoot is $\alpha_{\rm ov} = 0.31$–0.32. Thus, as with grid A, grid B indicates that sizeable overshoot mixing is required to match the

Table 2
Deduced Physical Properties of Two Best Asteroseismic Models from Grids A and B (in Table 1)

Parameter		
Model Name	mA	mB
Grid	A	B
$\chi^2_{\rm red}$	1808	3647
$M_{\rm ini}$ ($M_\odot$)	3.25 (5)	3.00 (5)
$Z_{\rm ini}$	0.020 (1)	0.023 (1)
Overshoot	$f_{\rm ov} = 0.024$ (1)	$\alpha_{\rm ov} = 0.32$ (1)
$\log D_{\rm ext}$ (cm^2 s^{-1})	0.75 (25)	0.50 (25)
X_c	0.503 (1)	0.496 (1)
$f_{\rm rot}^{\rm (opt)}$ (day^{-1})	0.4805	0.4744
$f_{\rm rot}^{\rm (opt)}/f_{\rm crit}$ (%)	26.4	26.6
$M_\star$ ($M_\odot$)	3.2499	3.0000
$R_\star$ ($R_\odot$)	2.7895	2.7501
$L_\star$ ($L_\odot$)	110.8	75.0
Age (10^6 year)	202	278
$m_{\rm cc}$ ($M_\odot$)	0.6215	0.5437
$r_{\rm cc}$ ($R_\odot$)	0.3356	0.3109
$m_{\rm ov}$ ($M_\odot$)	0.2642	0.2239
$r_{\rm ov}$ ($R_\odot$)	0.0558	0.0495

Note. Uncertainties in the grid parameters are set by the minimum stepsize in Table 1 and given in parentheses, which is a lower limit of the true uncertainty. Refer to Figure 2(b) and (c) for the extent of each mixing region in both models.

observations. Furthermore, the extra diffusive mixing is also constrained to $\log D_{\rm ext} = 0.50$–0.75, which is in excellent agreement with $\log D_{\rm ext} = 0.75$ found in grid A. In contrast with grid A (Figure 6), constraining the initial mass, metallicity, and age from grid B is less conclusive, and a broader range of values provides equally good overall frequency fits. Figure 2(c) shows the mixing property of the best model in grid B.

Figure 8(a) shows the resulting period spacing of "the best model" (black filled circles) from mA compared to the observations (gray symbols, from Figure 1). The overall fit to the slope of the period spacing is excellent, thanks to the optimized rotation frequency $f_{\rm rot}^{\rm (opt)}$. More importantly, the local dips in the observed period spacing are reasonably reproduced, mainly for the shorter-period modes. Toward the longer-period end (with increasing radial order), the quality of the fit noticeably degrades. Figure 8(b) shows the relative frequency difference between models and observations $\delta f_i/f_i^{\rm (obs)}$, where $\delta f_i = f_i^{\rm (obs)} - f_i^{\rm (mod)}$. All of the values are below 1%, and so the agreement between the observed and theoretical frequencies is at this level. The presence of the strong cyclic pattern in δf_i, among other things, hints at the possible presence of a glitch in the Brunt–Väisälä frequency which is not accounted for in our current treatment of the overshooting mixing. The reason for this, as already elaborated upon above, is the inadequacy of our knowledge about the convective boundary mixing by overshooting, and the missing physics in our 1D models which render the thermal and chemical stratification above the fully mixed core.

The inferred mean rotation frequency for mA is 26.4% of the Roche critical rotation frequency $f_{\rm crit}^{\rm (Rch)}$, which is defined as

$$f_{\rm crit}^{\rm (Rch)} = \frac{1}{2\pi}\left(\frac{8}{27}\frac{G\,M_\star}{R_\star^3}\right)^{1/2}, \quad (8)$$

where G, $M_\star$, and $R_\star$ are, respectively, the gravitational constant, stellar mass, and radius from the best non-rotating 1D model. KIC 7760680 is thus a moderately rotating SPB star. The corresponding estimate of the mean equatorial rotation velocity $v_{\rm eq} = 2\pi R_\star < f_{\rm rot} > \approx 63\,{\rm km\,s^{-1}}$, which agrees remarkably with the projected rotation velocity $v \sin i = 62 \pm 5\,{\rm km\,s^{-1}}$. This means that the inclination angle is $i \approx 80°$ and KIC 7760680 is observed nearly equator on, which is totally compatible with the detected sectoral ($m \neq 0$) modes.

Previously, we demonstrated that the exponentially decaying overshoot prescription provided a superior frequency fit to the observed modes of Star I (see Table 3 in Moravveji et al. 2015). The reason was that the corresponding $\chi^2_{\rm red}$ for the best step-function overshoot model was roughly 2.2 times worse (larger) than that from the exponentially decaying overshoot grid. We repeat the same exercise here, thanks to the extensive Step-Function grid (B) we computed (Table 1). The $\chi^2_{\rm red}$ for the step-function overshoot model from Table 2 is approximately twice that of the exponential overshoot. This is the second case for which the exponential overshoot prescription is favored over the classical step-function overshoot.

Table 2 summarizes the physical properties of the two best models from grids A and B. Despite different $\chi^2_{\rm red}$ scores, their associated parameters display interesting similarities, even when adopting two different overshooting prescriptions. The initial mass and metallicity of both models are found reasonably close; the lower-mass model has higher metallicity, and vice versa. This is the well-established $M_{\rm ini}$–$Z_{\rm ini}$ correlation, also shown in Ausseloos et al. (2004) for ν Eri, in Briquet et al. (2007) for θ Oph, and in Moravveji et al. (2015) for Star I. The core hydrogen content X_c and rotation frequency are found to be consistently close in both models. Most importantly, very low extra diffusive mixing $D_{\rm ext}$ is required in both models. Therefore, the global properties of the star, inferred from our seismic modeling, weekly depend on the adopted overshoot model. Regardless of the overshoot prescription option, both models point to a sizeable amount of overshoot in the presence of rotation. This strengthens our earlier conclusion that moderate rotation requires larger core overshooting than for slow rotation.

In Table 2, we give the mass contained in the fully mixed convective core $m_{\rm cc}$, the mass contained in the overshooting region $m_{\rm ov}$, and their radial extents $r_{\rm cc}$ and $r_{\rm ov}$, respectively, from the profiles of the equilibrium structure. The relative extent of the overshooting regions in both models (Table 2) are almost identical. The relative overshooting mass with respect to the star mass $m_{\rm ov}/M_\star$ in mA (or mB) is 8.1% (or 7.5%). In terms of radial extent, $r_{\rm ov}/R_\star$ for the mA (or mB) is 2.0% (or 1.8%). Although the overshoot region is a narrow part of the star, we show in Section 8.3 that many high-order g-modes are perfectly trapped inside this layer. Similarly, we can compare the relative mass and radial extent of the overshoot zone with respect to that of the convective core to shed light on the distance over which the convective eddies travel before losing their identity and falling back. For mA (or mB), $m_{\rm ov}/m_{\rm cc}$ is 42.5% (or 41.2%), and similarly $r_{\rm ov}/r_{\rm cc}$ is 16.6% (or 15.9%). Therefore, the fully mixed cores in late B-type stars require ~16% increase in mass beyond their canonical boundary from the MLT. We argue that future, more advanced non-local time-dependent theories of convection (Xiong 1979, 1989; Canuto 2011a, 2011b; Zhang & Li 2012b; Zhang 2013, 2016; Arnett et al. 2015) should closely reproduce our seismic

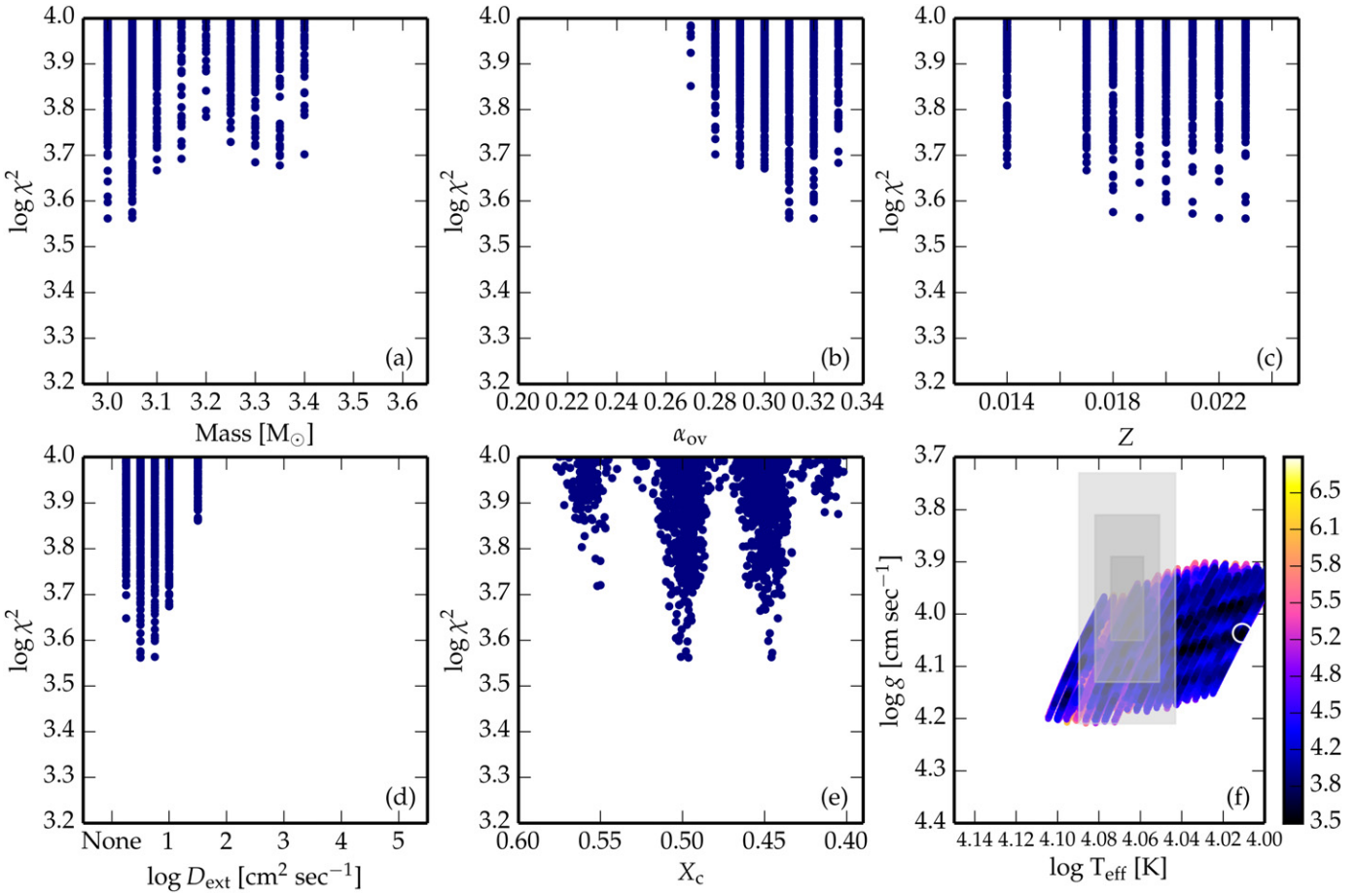

Figure 7. Similar to Figure 6, but for the grid B with step-function overshooting. The ordinate of the two figures are identical.

findings. Three-dimensional (3D) simulations by Browning et al. (2004) for rotating A-type stars have already predicted that convective cores require at least $d_{\rm ov} \gtrsim 0.20\,H_p$ overshoot extension beyond the canonical boundary, depending on the stiffness (buoyancy jump) of the stratification. The need for such core extension in our results agrees with the predictions of Browning et al.

The relative frequency deviations $\delta f_i / f_i^{\rm (obs)}$ for model mA is below 1%. This is clearly shown in Figure 8(b). For Star I, this was below 0.3%, which is a factor of three better than KIC 7760680. Therefore, our seismic models serve as the perfect starting point for frequency inversion of the gravity modes in order to improve the assumed thermal and chemical stratification of the overshooting, beyond the current available models. Although the structure inversion theory for solar-type p-mode pulsators is well established (see Basu 2014; Buldgen et al. 2015, and references therein), no such theory has yet been developed for heat-driven, high-order g-modes in massive stars.

8.2. Non-adiabatic Mode Stability

As an a posteriori test, we consider the mode stability properties by computing the non-adiabatic dipole prograde frequencies (Townsend 2005a, 2005b). For the best model, the radial order of the modes that match the observation lie in the range $-53 \leqslant n_{\rm pg} \leqslant -18$. Figure 9 shows the normalized growth rate $\eta = W / \int_0^{R_\star} |dW|$ for the best model, as first introduced by Stellingwerf (1978). Here, W is the total work, derived by integrating the work integrand dW over the whole star $W = \int_0^{R_\star} dW$. Unstable (stable) modes correspond to positive (negative) η values, and are shown with filled (or empty) squares. From $\mathcal{N} = 36$ modes, a total of 34 modes are predicted to be unstable, which is in excellent agreement with observations, thanks to employing OP tables with enhanced Fe and Ni monochromatic opacities. Ignoring the important role of Fe and Ni drastically underestimates the predicted excited modes (Dziembowski & Pamyatnykh 2008; Salmon et al. 2012). Therefore, in addition to solving the β Cep and hybrid pulsating massive stars excitation problem presented in Moravveji (2016), the success in explaining the excitation of the majority of observed modes by incorporating Fe and Ni monochromatic opacity enhancement is another manifestation that the default (OP and OPAL) opacity tables underestimate the Rosseland mean opacity in stellar interiors. Consequently, the stellar interior seems to be more opaque than was believed, and the next generation of stellar models should adopt the updated tables of Moravveji (2016) and/or Mondet et al. (2015).

In Figure 9, the period instability domain does not perfectly agree with observations, and seems to be shifted toward lower-order modes: five short-period g-modes are predicted to be unstable but are not observed, in addition to seven long-period g-modes that are observed, but are predicted to be stable. We previously found a similar issue for Star I; see Figure 9 in Moravveji et al. (2015).

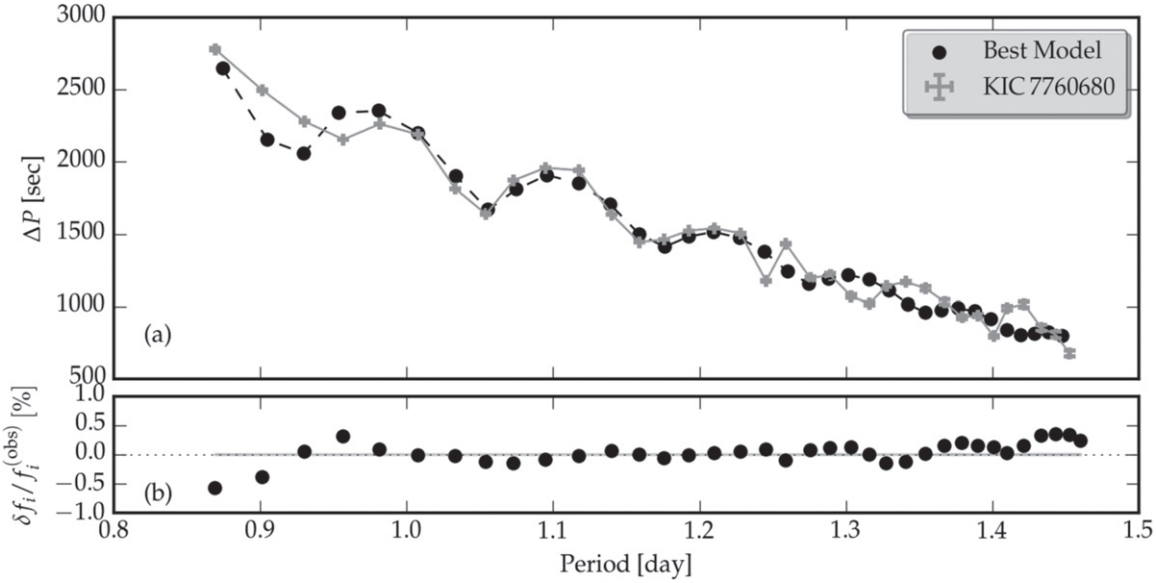

Figure 8. (a) Comparing period spacing from observations (gray) vs. the best-fit model (black) from grid A. The parameters of this model are given in Table 2. For a comparison with Star I, refer to Figure 4 in Moravveji et al. (2015). The two patterns reasonably match up to ∼1.23 day^{-1}, beyond which the two start to deviate. (b) Percentage of relative frequency difference between the observation and the model, $\delta f_i/f_i^{(\mathrm{obs})}$. The narrow gray area in the middle is the observed 1σ uncertainty shown in Figure 1(b). Note the presence of a cyclic pattern in $\delta f_i/f_i^{(\mathrm{obs})}$.

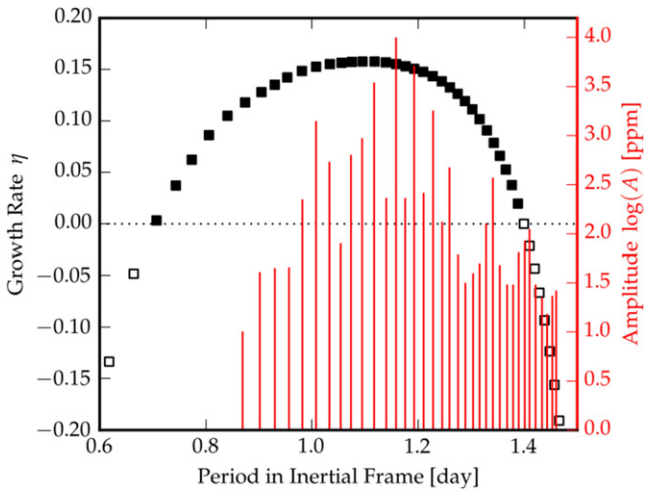

Figure 9. Normalized growth rates η for the best model. The unstable (stable) modes are presented with black filled (empty) squares. The logarithm of the observed mode amplitude A of the dipole series is shown with vertical red lines.

We speculate that the slight mismatch in Figure 9 between the observed and predicted excited modes can possibly be explained by any, or the combination of, the following three missing physical inputs in the current 1D evolutionary models. (1) First, gravitational settling and radiative levitation are ignored in our 1D models (due to their ∼100 times longer computation overhead). The 3D and 1D simulations of Zemskova et al. (2014) for a 1.5 $M_\odot$ star showed that Fe can gradually accumulate in the iron bump, modifying the local metallicity without a noticeable change of the surface metallicity. With KIC 7760680 having more than twice the mass contained in the simulations of Zemskova et al., radiative levitation can dominate even further and contribute very efficiently to iron and nickel accumulation around the iron bump. This important feature is still missing from our MESA models. (2) Second, the Fe and Ni are the major contributors to the iron opacity bump, whose abundance in KIC 7760680 are assumed to be solar. This may not necessarily be true. Thus, a slight increase in the Fe and Ni initial abundance (at the cost of a slight reduction in initial hydrogen and/or helium) can potentially resolve this problem. This is beyond the scope of our current paper because it calls for re-computing (even a part of) our asteroseismic grid for unknown initial chemical mixtures, X_i, for i = H, He, …, Fe, Ni. (3) Third, the iron opacity peak occurs around $\log T \approx 5.2$–5.3 dex. We speculate that a slight inward shift of the opacity peak toward the hotter interior can help to overcome radiative damping, and alleviate the lack of sufficient excited modes.

8.3. Mode Trapping in the Deep Stellar Interior

It is instructive to consider the modal behavior (of our best model) to demonstrate the probing power of high-order g-modes in the deep stellar interior. The rotational kernels $\mathcal{K}_{n,\ell}$ and mode inertia $\mathcal{I}_{n,\ell}$—which are constructed from the radial and horizontal components of eigendisplacements and defined in Aerts et al. (2010)—are two useful quantities to exploit. The kernels of high-order g-modes become progressively oscillatory with the increase in mode radial order (and mode period), and attain a larger amplitude toward the core compared to the surface. This makes high-order g-modes in rotating SPB stars ideal probes of the near-core environment, provided that the local wavelength of the mode is roughly equal to or smaller than the length scale of the change of structure in the background model (Belyaev et al. 2015; Cunha et al. 2015). In such cases, the model g-modes are able to *resolve* the structure of their background medium (which they propagate in), and their frequencies reveal the shortcomings in treating the near-core thermal and chemical stratification by deviating from observations. We argue that a subset of g-modes in KIC 7760680 are trapped inside the overshoot region, and reveal that the current states of the modeling of chemical mixing and thermal stratification in that region are not accurate enough to explain the high precision data.

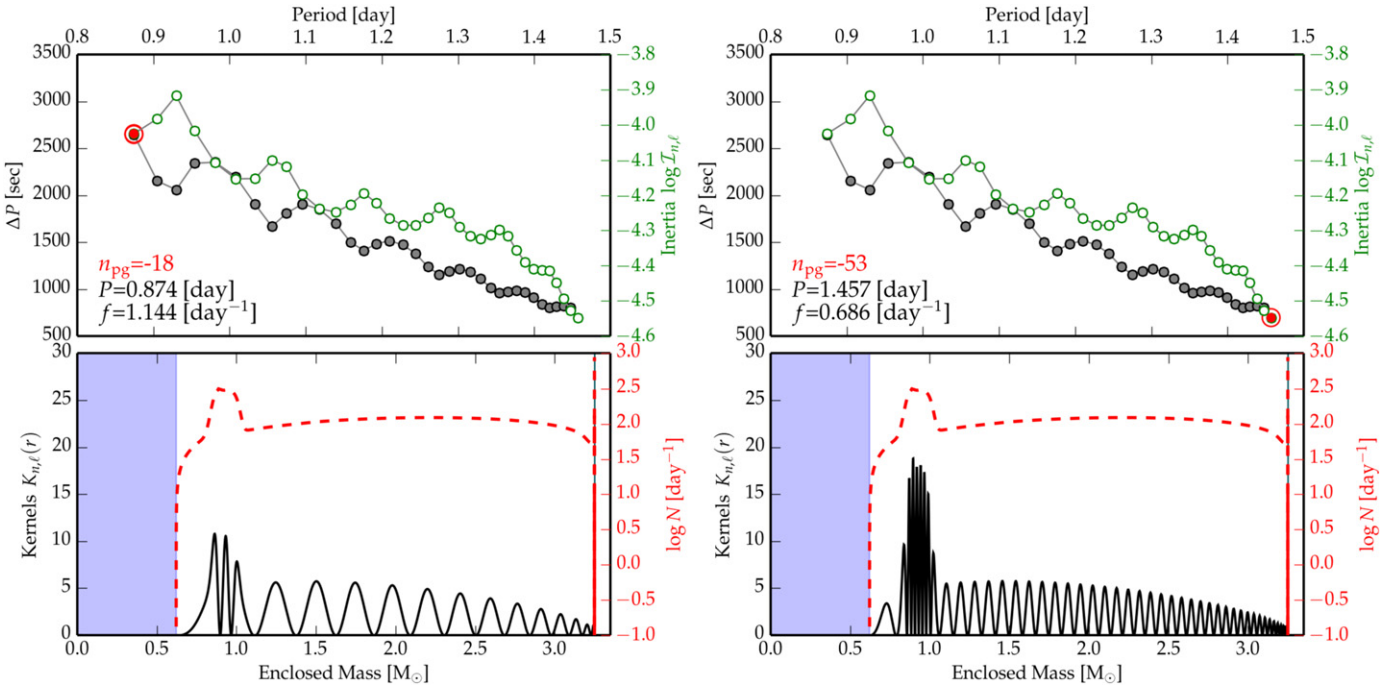

Figure 10. Mode Kernels $\mathcal{K}_{n,\ell}$ (bottom solid line) and the logarithm of mode inertia $\mathcal{I}_{n,\ell}$ (top empty dots) for the shortest-period mode with period $P_1 = 0.873$ day^{-1} (left), and for the longest-period mode with period $P_{36} = 1.457$ day^{-1} (right). In the top panels, the period spacing is shown by gray filled dots. The red empty circles mark the corresponding mode. On the bottom panels, the blue area shows the convective core where g-modes are evanescent, and the red dashed line shows the Brunt–Väisälä frequency $\log N$. The best model from Table 2 is used as input.

The two panels in Figure 10 compare several seismic properties of the lowest-order g-mode $n_{pg} = -18$ (left) and the highest-order one $n_{pg} = -53$ (right) in the best model. They represent the two extreme mode behaviors in the observed series, while those of the intermediate modes exhibit a smooth transition between the two shown here. The top panels show the period spacing (filled dots) and mode inertia (empty dots) versus mode periods. The bottom panels show the profile of normalized rotational kernels $K_{n,\ell}$; in this panel, the convective zone is highlighted in blue, and the Brunt–Väisälä frequency is shown with a dashed red line.

The kernels exhibit two significant features on top of the convective core: (a) both modes exhibit partial trapping in the μ-gradient region—associated with the broad bump in the Brunt–Väisälä frequency. The kernels of the modes associated with the dips in the period spacing attain highest relative amplitude in the μ-gradient region and become fully trapped. (b) The kernels of the modes with radial order exceeding ~30, i.e., $n_{pg} \lesssim -30$, exhibit additional trapping in the overshooting region between the boundary of the convective core and the base of the bump in the Brunt–Väisälä frequency. Note the final emergence of a fully trapped mode in the bottom left panel in Figure 10 at the mass coordinate $m \approx 0.75\,M_\odot$. The highest-order modes which exhibit this additional trapping are those which probe the overshoot zone and provide very precise diagnostics of the physical structure of this region.

Consequently, the entire series of identified g-modes of KIC 7760680 allow us to exploit the extent and physical conditions of chemically homogeneous (overshooting) and inhomogeneous (μ-gradient) layers in massive stars. The success (failure) in matching the individual observed frequencies is a reward (penalty) of the accuracy of our current understanding and implementation of the physics of the stellar interior. The fact that lower-order modes ($n_{pg} \gtrsim -30$) better match the observation is clear evidence that the structure of the μ-gradient layer is well represented in our 1D evolutionary model. However, the evident period spacing deviations of higher-order modes ($n_{pg} \lesssim -30$) from observations unambiguously indicates a lack of missing physics of the overshoot mixing. This explains the cyclic deviations between frequencies of the best model from observations presented in Figure 8(b). This can be attributed to the ad hoc implementation of overshoot (e.g., Section 3) in 1D models, since our local, time-averaged description of convective mixing by MLT does not consistently account for convection-induced mixing beyond the core boundaries (e.g., Browning et al. 2004; Arnett 2014 and references therein).

The non-local, time-dependent convective models (see, e.g., Xiong 1979, 1989; Canuto 2011a, 2011b; Zhang & Li 2012b; Zhang 2013, 2016; Pasetto et al. 2014, 2015; Arnett et al. 2015) may be able to provide better insight into the physical structure of the overshoot region, and allow us to improve the fit to the observed period spacing of g-mode pulsators. Therefore, the long series of dipole period spacing in KIC 7760680 and Star I provides two ideal tests for theories of convective and non-convective heat, as well as chemical and angular momentum transport.

9. SUMMARY, DISCUSSION, AND CONCLUSIONS

Let us revisit and discuss the four questions raised in Section 1. In this paper, we carried out a thorough forward seismic modeling of KIC 7760680, the richest SPB star discovered so far. We computed two non-rotating MESA grids and incorporated the effect of rotation on g-modes by employing the traditional approximation. The unknown equatorial rotation frequency of the target was varied and optimized by forcing it to match the exact number of dipole

prograde modes within the observed range; this approach automatically reproduces the negative slope in the observed period spacing. All of the models in our grids were ranked by a $\chi^2_{\rm red}$ merit function that accounted for the fitting of the frequencies. We showed that KIC 7760680 is a 3.25 $M_\odot$ SPB star that rotates at ~26% of its Roche break up frequency. At this moderate rotation velocity, substantial overshoot is required to match the frequencies. Therefore, we demonstrate that rotation increases convective overshooting from the core compared to the non-rotating case.

Considering Star I, we managed to tightly constrain $f_{\rm ov}$ to ~0.017 and favored the exponential prescription over the step-function. It is worth noting that the diffusive exponential prescription is also supported by the time-dependent convection model of Zhang (2013), Zhang & Li (2012a), and Zhang (2016, and the references therein), which contradicts the predictions of Zahn (1991) and Viallet et al. (2015) that core overshooting results in an adiabatic extension of the core. Our seismically derived overshoot values for the best models are $f_{\rm ov} = 0.024$ and $\alpha_{\rm ov} = 0.32$. These are in excellent agreement with the previous studies (reviewed by Aerts 2013 and the references therein), in addition to those of Stancliffe et al. (2015) from fitting the global observables of nine binary systems, between 1.3 and 6.2 $M_\odot$, and the seismic modeling of Deheuvels et al. (2016) for F stars at the onset of convective cores. Thus, a global picture of overshoot mixing for a broad range of stellar masses is gradually emerging.

We allowed substantial mixing in the radiative regions as we chose to vary $D_{\rm ext}$ from zero up to 10^5. We found values at least an order of magnitude smaller compared to the theoretical predictions of Mathis et al. (2004). If shear-induced turbulent mixing was important in KIC 7760680, then our seismic models—through their $\chi^2_{\rm red}$ scores—should have preferred higher values for $\log D_{\rm ext}$. From Figure 6(d), this is obviously not the case. Since the shear-induced mixing depends explicitly on the gradient of the angular velocity, we infer that such a gradient is small, if not zero, and the upper limit of the resulting effective diffusion transport coefficient is roughly $D_{\rm ext} \lesssim 10$. The absence of differential rotational and shear-induced mixing is strong evidence that KIC 7760680 is most probably rotating rigidly. This is quite acceptable in light of finding small shear in two *Kepler* F-type stars (Kurtz et al. 2014; Saio et al. 2015). In fact, heat-driven g-modes (Lee & Saio 1993) and stochastically excited internal gravity waves (Rogers 2015) are predicted to efficiently redistribute angular momentum inside B-type stars and induce near-rigid rotation. KIC 7760680 could be another manifestation of this. In the meantime, we cannot exclude other possible mechanisms that can suppress mixing and enforce rigid-body rotation. In light of recent advancements in asteroseismology, deep-rooted fossil magnetic fields turn out to be ubiquitous in intermediate, main-sequence stars (Stello et al. 2016) and their red giant descendants (Fuller et al. 2015). Asteroseismic modeling of the the magnetic β Cep pulsator V 2052 Ophiuchi by Briquet et al. (2012) revealed that an internal magnetic field can suppress core overshoot. In addition, Briquet et al. (2016) showed that the weakly magnetic B2 IV-V SPB star ζ Cas rotates rigidly with a magnetic field of strength 100–150 G inhibiting mixing in its envelope. The observed nitrogen enhancement was then attributed to transport by internal gravity waves. Because KIC 7760680 is an intermediate-mass star, it can be a showcase of the magnetic inhibition of chemical mixing by rigid rotation.

We inferred (in Section 8.1) that KIC 7760680 is nearly a solid body rotator because the extra diffusive mixing is limited to $\log D_{\rm ext} \approx 0.75$. This is not surprising. The two γ Dor stars (which are similarly high-order, low-degree g-mode pulsators with roughly half the mass of KIC 7760680) studied by Kurtz et al. (2014) and Saio et al. (2015) unambiguously exhibit core-to-surface rotation frequency close to unity based on the frequency splittings of their p- and g-modes. Star I was also shown to be a very slowly rotating star with a counter-rotating envelope with respect to its core (Triana et al. 2015). Rogers (2015) successfully explained all of these observed cases through very efficient angular momentum transport carried by internal gravity waves (see also Zahn et al. 1997; Talon & Charbonnel 2005; Rogers et al. 2013). The same mechanism is used by Aerts & Rogers (2015) to explain the observed background power excess in the periodograms of three CoRoT O-type dwarfs. Therefore, in dwarf stars earlier than A-type, the angular momentum transport can be more efficient than predicted, and it can impose near-rigid envelope rotation.

The two recently modeled *Kepler* SPB stars, Star I and KIC 7760680, are the best-understood stars of their class. Their constrained physical parameters can serve as a starting point for more sophisticated and/or realistic theories of energy and chemical transport by turbulent convection beyond MLT. In fact, more realistic future convection models should succeed in improving the fitting of the observed frequencies of these two SPB stars, in addition to surviving the helioseismic tests.

The authors are grateful to Peter I. Pápics for the reanalysis of the light curve, and for determining the correction factor to be applied for frequency uncertainties ($Q = 4.0$) compared to those derived from NLLS. The research leading to these results has received funding from the People Programme (Marie Curie Actions) of the European Union's Seventh Framework Programme FP7/2007–2013/ under REA grant agreement No. 623303 (ASAMBA), from the European Research Council (ERC) under the European Union's Horizon 2020 research and innovation programme grant No. 670519 (MAMSIE), and from the European Community's Seventh Framework Programme FP7-SPACE-2011-1, project No. 312844 (SPACEINN). R.H. D.T. acknowledges support from NSF under the SI^2 program grants (ACI-1339600) and NASA under the TCAN program grants (NNX14AB55G). S.M. acknowledges funding by ERC grant No. 647383 (SPIRE). The computational resources and services used in this work were provided by the VSC (Flemish Supercomputer Center), funded by the Hercules Foundation and the Flemish Government—department EWI.

APPENDIX A
DISTINGUISHING HARMONIC DEGREE AND AZIMUTHAL ORDER

Figure 11 shows eight period spacing series for dipole and quadrupole modes using TAR. The input model fulfills the position of the star on the Kiel diagram, and is set to uniform rotation with 24.2% with respect to the Roche critical frequency (Equation (8)). The observed ΔP pattern (red line) is well reproduced by dipole prograde modes, while all of the other spacings fail to satisfy Equation (5) and match the slope of the period spacing. Moreover, extremely high radial orders of up to $|n_{\rm pg} \approx 700|$ were needed for $(\ell, m) = (2, 1)$ and $(2, 2)$ to force them toward the observed range, which contradicts the

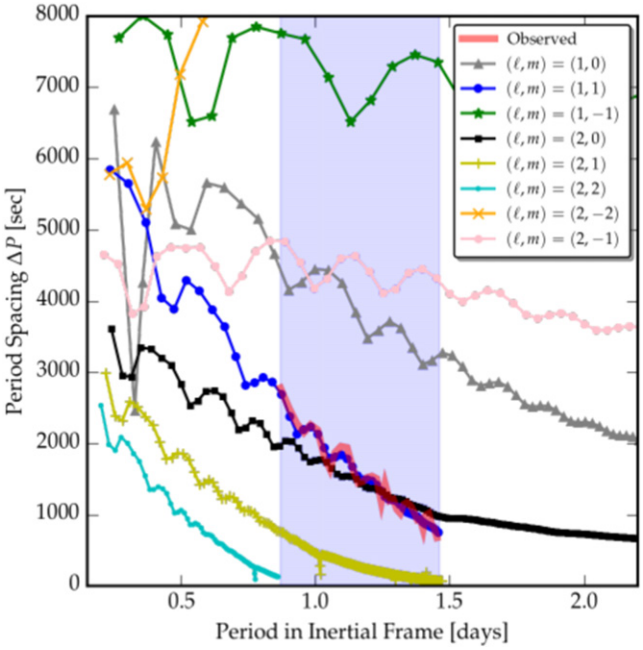

Figure 11. Period spacing ΔP for eight combinations of (ℓ, m) for dipole and quadrupole modes, compared with the observed series (red solid line). The input model is set to ∼24% rotation frequency with respect to $f_{\rm rot}^{\rm (Rch)}$.

requirement $\mathcal{N} = 36$. Thus, the observed series in Figure 1(a) is identified as dipole prograde $(\ell, m) = (1, +1)$ g-modes.

APPENDIX B
DELIVERABLES, INLISTS, AND OPACITY TABLES

Following the MESA users' code of conduct stated in Paxton et al. (2011), we publish the MESA and GYRE inlists, and the structure file of the best asteroseismic model of KIC 7760680 (compatible with GYRE). This ensures the reproducibility of our results, provided similar MESA and GYRE versions are used. These products are availble through the following static link: https://fys.kuleuven.be/ster/Projects/ASAMBA. The adopted OP opacity tables are already available from https://bitbucket.org/ehsan_moravveji/op_mono.

APPENDIX C
ITERATIVE PROCEDURE TO OPTIMIZE $f_{\rm rot}$

Here, we explain the iterative procedure to optimize $f_{\rm rot}$ (or equivalently $\eta_{\rm rot}$) using Equations (4) and (5). Figure 12 illustrates the procedure. The first attempt corresponds to a small trial $f_{\rm rot}$, and the second one corresponds to a much larger trial value for $f_{\rm rot}$, ensuring a change of sign of $d\mathcal{N}$. For the third attempt, we estimate $f_{\rm rot}$ by Newton–Raphson root-finding, assuming a line connecting the first two points. From the fourth attempt onward, we use the Van Wijngaarden–Dekker–Brent (Brent 1973) root-finding algorithm to locate the zero of $d\mathcal{N}$ (see also Press et al. 2007). The iterations proceed until the root is successfully located. Considering the fact that $d\mathcal{N}$ is an integer-valued function, it seldom happens that a tiny change in $f_{\rm rot}$ proposed by the previous (Brent) guess does not change $\mathcal{M}$. In such cases, $d\mathcal{N}$ is zero (has a staircase shape) and the Brent scheme diverges. To avoid such circumstances, we employ an iterative Bisection method (Press et al. 2007) to converge to the root of $d\mathcal{N}$. During all of these attempts, we call GYRE, and store the intermediate results on the disk, until

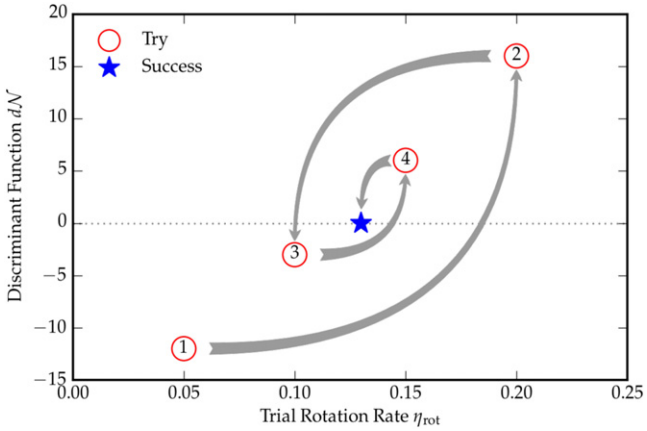

Figure 12. Scheme for optimizing $\eta_{\rm rot} = f_{\rm rot}/f_{\rm rot}^{\rm (Rch)}$.

the procedure succeeds. Finally, we store the optimal rotation frequency $f_{\rm rot}^{\rm (opt)}$ as an additional attribute in the GYRE output summary file.

REFERENCES

Aerts, C. 2013, EAS Publications Ser. 64, Setting a New Standard in the Analysis of Binary Stars, ed. K. Pavlovski, A. Tkachenko, & G. Torres (Noordwijk: ESA), 323
Aerts, C., Christensen-Dalsgaard, J., & Kurtz, D. W. 2010, Asteroseismology (Berlin: Springer)
Aerts, C., Lamers, H. J. G. L. M., & Molenberghs, G. 2004, A&A, 418, 639
Aerts, C., & Rogers, T. M. 2015, ApJL, 806, L33
Aprilia, Lee, U., & Saio, H. 2011, MNRAS, 412, 2265
Arnett, W. D. 2014, in New Windows on Massive Stars: Asteroseismology, Interferometry and Spectropolarimetry, ed. G. Meynet et al. (Cambridge: Cambridge Univ. Press), 459
Arnett, W. D., Meakin, C., Viallet, M., et al. 2015, ApJ, 809, 30
Asplund, M., Grevesse, N., Sauval, A. J., & Scott, P. 2009, ARA&A, 47, 481
Ausseloos, M., Scuflaire, R., Thoul, A., & Aerts, C. 2004, MNRAS, 355, 352
Badnell, N. R., Bautista, M. A., Butler, K., et al. 2005, MNRAS, 360, 458
Bailey, J. E., Nagayama, T., Loisel, G. P., et al. 2015, Natur, 517, 56
Ballot, J., Lignières, F., Prat, V., Reese, D. R., & Rieutord, M. 2012, in ASP Conf. Ser. 462, Progress in Solar/Stellar Physics with Helio- and Asteroseismology, ed. H. Shibahashi, M. Takata, & A. E. Lynas-Gray (San Francisco, CA: ASP), 389
Ballot, J., Lignières, F., Reese, D. R., & Rieutord, M. 2010, A&A, 518, A30
Balona, L. A., Pigulski, A., Cat, P. D., et al. 2011, MNRAS, 413, 2403
Basu, S. 2014, Studying Stars Through Frequency Inversions, ed. P. L. Pallé, & C. Esteban (Cambridge Univ. Press), 87
Belyaev, M. A., Quataert, E., & Fuller, J. 2015, MNRAS, 452, 2700
Böhm-Vitense, E. 1958, ZAp, 46, 108
Bouabid, M.-P., Dupret, M.-A., Salmon, S., et al. 2013, MNRAS, 429, 2500
Brent, R. P. 1973, Algorithms for Minimization Without Derivatives (Englewood Cliffs, NJ: Prentice-Hall)
Briquet, M., Morel, T., Thoul, A., et al. 2007, MNRAS, 381, 1482
Briquet, M., Neiner, C., Aerts, C., et al. 2012, MNRAS, 427, 483
Briquet, M., Neiner, C., Petit, P., et al. 2016, A&A, 587, A126
Browning, M. K., Brun, A. S., & Toomre, J. 2004, ApJ, 601, 512
Buldgen, G., Reese, D. R., & Dupret, M. A. 2015, A&A, 583, A62
Canuto, V. M. 2011a, A&A, 528, A76
Canuto, V. M. 2011b, A&A, 528, A80
Castelli, F., & Kurucz, R. L. 2003, in IAU Symp. 210, Modelling of Stellar Atmospheres, ed. N. Piskunov, W. W. Weiss, & D. F. Gray (San Francisco, CA: ASP), A20
Cox, J. P., & Giuli, R. T. (ed.) 1968, Principles of Stellar Structure (New York: Gordon and Breach)
Cunha, M. S., Stello, D., Avelino, P. P., Christensen-Dalsgaard, J., & Townsend, R. H. D. 2015, ApJ, 805, 127
De Cat, P., & Aerts, C. 2002, A&A, 393, 965
Decressin, T., Mathis, S., Palacios, A., et al. 2009, A&A, 495, 271
Degroote, P., Briquet, M., Catala, C., et al. 2009, A&A, 506, 111
Deheuvels, S., Brandão, I., Silva Aguirre, V., et al. 2016, arXiv:1603.02332
Dintrans, B., & Rieutord, M. 2000, A&A, 354, 86

Dufton, P. L., Langer, N., Dunstall, P. R., et al. 2013, A&A, 550, A109
Dziembowski, W. A., & Goode, P. R. 1992, ApJ, 394, 670
Dziembowski, W. A., Moskalik, P., & Pamyatnykh, A. A. 1993, MNRAS, 265, 588
Dziembowski, W. A., & Pamyatnykh, A. A. 1991, A&A, 248, L11
Dziembowski, W. A., & Pamyatnykh, A. A. 2008, MNRAS, 385, 2061
Eckart, C. 1960, Hydrodynamics of Oceans and Atmospheres (Oxford: Pergamon)
Endal, A. S., & Sofia, S. 1976, ApJ, 210, 184
Endal, A. S., & Sofia, S. 1978, ApJ, 220, 279
Espinosa Lara, F., & Rieutord, M. 2013, A&A, 552, A35
Freytag, B., Ludwig, H.-G., & Steffen, M. 1996, A&A, 313, 497
Fuller, J., Cantiello, M., Stello, D., Garcia, R. A., & Bildsten, L. 2015, Sci, 350, 423
Gautschy, A., & Saio, H. 1993, MNRAS, 262, 213
Heger, A., Langer, N., & Woosley, S. E. 2000, ApJ, 528, 368
Heger, A., Woosley, S. E., & Spruit, H. C. 2005, ApJ, 626, 350
Herwig, F. 2000, A&A, 360, 952
Huang, W., Gies, D. R., & McSwain, M. V. 2010, ApJ, 722, 605
Huat, A.-L., Hubert, A.-M., Baudin, F., et al. 2009, A&A, 506, 95
Kippenhahn, R., & Thomas, H.-C. 1970, in IAU Coll. 4: Stellar Rotation, ed. A. Slettebak (New York: Gordon and Breach), 20
Kurtz, D. W., Saio, H., Takata, M., et al. 2014, MNRAS, 444, 102
Langer, N., El Eid, M. F., & Fricke, K. J. 1985, A&A, 145, 179
Ledoux, P. 1951, ApJ, 114, 373
Lee, U., Mathis, S., & Neiner, C. 2016, MNRAS, 457, 2445
Lee, U., Neiner, C., & Mathis, S. 2014, MNRAS, 443, 1515
Lee, U., & Saio, H. 1986, MNRAS, 221, 365
Lee, U., & Saio, H. 1993, MNRAS, 261, 415
Lee, U., & Saio, H. 1997, ApJ, 491, 839
Maeder, A. 1975, A&A, 40, 303
Maeder, A. (ed.) 2009, Physics, Formation and Evolution of Rotating (Berlin: Springer-Verlag)
Maeder, A., Meynet, G., Lagarde, N., & Charbonnel, C. 2013, A&A, 553, A1
Maeder, A., & Zahn, J.-P. 1998, A&A, 334, 1000
Mathis, S. 2013, in Studying Stellar Rotation and Convection: Theoretical Background and Seismic Diagnostics, ed. M. Goupil et al. (Berlin: Springer)
Mathis, S., Neiner, C., & Tran Minh, N. 2014, A&A, 565, A47
Mathis, S., Palacios, A., & Zahn, J.-P. 2004, A&A, 425, 243
Mathis, S., Talon, S., Pantillon, F.-P., & Zahn, J.-P. 2008, SoPh, 251, 101
Mathis, S., & Zahn, J.-P. 2004, A&A, 425, 229
Mathis, S., & Zahn, J.-P. 2005, A&A, 440, 653
Meynet, G., & Maeder, A. 2000, A&A, 361, 101
Miglio, A., Montalbán, J., Noels, A., & Eggenberger, P. 2008, MNRAS, 386, 1487
Mondet, G., Blancard, C., Cossé, P., & Faussurier, G. 2015, ApJS, 220, 2
Moravveji, E. 2015, EAS Publications Ser. 71, New Windows on Massive Stars, ed. G. Meynet et al. (Cambridge: Cambridge Univ. Press), 317
Moravveji, E. 2016, MNRAS, 455, L67
Moravveji, E., Aerts, C., Pápics, P. I., Triana, S. A., & Vandoren, B. 2015, A&A, 580, A27
Nagayama, T., Bailey, J. E., Loisel, G., et al. 2016, PhRvE, 93, 023202
Neiner, C., Floquet, M., Samadi, R., et al. 2012, A&A, 546, A47
Nieva, M.-F., & Przybilla, N. 2012, A&A, 539, A143
Pamyatnykh, A. A. 1999, AcA, 49, 119
Pantillon, F. P., Talon, S., & Charbonnel, C. 2007, A&A, 474, 155
Pápics, P. I., Briquet, M., Auvergne, M., et al. 2011, A&A, 528, A123
Pápics, P. I., Briquet, M., Baglin, A., et al. 2012, A&A, 542, A55
Pápics, P. I., Moravveji, E., Aerts, C., et al. 2014, A&A, 570, A8
Pápics, P. I., Tkachenko, A., Aerts, C., et al. 2015, ApJL, 803, L25
Pasetto, S., Chiosi, C., Chiosi, E., Cropper, M., & Weiss, A. 2015, arXiv:1511.08811
Pasetto, S., Chiosi, C., Cropper, M., & Grebel, E. K. 2014, MNRAS, 445, 3592
Paxton, B., Bildsten, L., Dotter, A., et al. 2011, ApJS, 192, 3
Paxton, B., Cantiello, M., Arras, P., et al. 2013, ApJS, 208, 4
Paxton, B., Marchant, P., Schwab, J., et al. 2015, ApJS, 220, 15
Prat, V., Lignières, F., & Ballot, J. 2016, A&A, 587, A110
Press, W. H., Teukolsky, S. A., Vetterling, W. T., & Flannery, B. P. 2007, Numerical Recipes: The Art of Scientific Computing (3rd ed.; New York, NY, USA: Cambridge Univ. Press)
Puls, J., Sundqvist, J. O., & Markova, N. 2015, in IAU Symp. 307, ed. G. Meynet et al. (Cambridge Univ. Press), 25
Ramírez-Agudelo, O. H., Sana, H., de Mink, S. E., et al. 2015, A&A, 580, A92
Ramírez-Agudelo, O. H., Simón-Díaz, S., Sana, H., et al. 2013, A&A, 560, A29
Raskin, G., van Winckel, H., Hensberge, H., et al. 2011, A&A, 526, A69
Reese, D., Lignières, F., & Rieutord, M. 2006, A&A, 455, 621
Rogers, T. M. 2015, ApJL, 815, L30
Rogers, T. M., Lin, D. N. C., McElwaine, J. N., & Lau, H. H. B. 2013, ApJ, 772, 21
Roxburgh, I. W. 1965, MNRAS, 130, 223
Saio, H., & Deupree, R. G. 2012, in ASP Conf. Ser. 462, Progress in Solar/Stellar Physics with Helio- and Asteroseismology, ed. H. Shibahashi, M. Takata, & A. E. Lynas-Gray (San Francisco, CA: ASP), 398
Saio, H., Kurtz, D. W., Takata, M., et al. 2015, MNRAS, 447, 3264
Salmon, S., Montalbán, J., Morel, T., et al. 2012, MNRAS, 422, 3460
Savonije, G. J. 2005, A&A, 443, 557
Savonije, G. J. 2013, A&A, 559, A25
Schwarzenberg-Czerny, A. 1991, MNRAS, 253, 198
Seaton, M. J. 2005, MNRAS, 362, L1
Shibahashi, H., & Ishimatsu, H. 2013, Stellar Pulsations: Impact of New Instrumentation and New Insights, Vol. 31, ed. J. C. Suárez et al. (Berlin: Springer-Verlag), 49
Soufi, F., Goupil, M. J., & Dziembowski, W. A. 1998, A&A, 334, 911
Stancliffe, R. J., Fossati, L., Passy, J.-C., & Schneider, F. R. N. 2015, A&A, 575, A117
Stellingwerf, R. F. 1978, AJ, 83, 1184
Stello, D., Cantiello, M., Fuller, J., et al. 2016, Natur, 529, 364
Talon, S., & Charbonnel, C. 2005, A&A, 440, 981
Talon, S., Zahn, J.-P., Maeder, A., & Meynet, G. 1997, A&A, 322, 209
Tassoul, M. 1980, ApJS, 43, 469
Townsend, R. H. D. 2003a, MNRAS, 343, 125
Townsend, R. H. D. 2003b, MNRAS, 340, 1020
Townsend, R. H. D. 2005a, MNRAS, 360, 465
Townsend, R. H. D. 2005b, MNRAS, 364, 573
Townsend, R. H. D., & Teitler, S. A. 2013, MNRAS, 435, 3406
Triana, S. A., Moravveji, E., Pápics, P. I., et al. 2015, ApJ, 810, 16
Unno, W. et al. (ed.) 1989, Nonradial Oscillations of Stars (Tokyo: University of Tokyo Press)
Van Reeth, T., Tkachenko, A., Aerts, C., et al. 2015a, A&A, 574, A17
Van Reeth, T., Tkachenko, A., Aerts, C., et al. 2015b, ApJS, 218, 27
Viallet, M., Meakin, C., Prat, V., & Arnett, D. 2015, A&A, 580, A61
Vink, J. S., de Koter, A., & Lamers, H. J. G. L. M. 2001, A&A, 369, 574
Waelkens, C. 1991, A&A, 246, 453
Waelkens, C., Aerts, C., Kestens, E., Grenon, M., & Eyer, L. 1998, A&A, 330, 215
Xiong, D.-R. 1979, AcASn, 20, 238
Xiong, D.-R. 1989, A&A, 213, 176
Zahn, J.-P. 1991, A&A, 252, 179
Zahn, J.-P. 1992, A&A, 265, 115
Zahn, J.-P., Talon, S., & Matias, J. 1997, A&A, 322, 320
Zemskova, V., Garaud, P., Deal, M., & Vauclair, S. 2014, ApJ, 795, 118
Zhang, Q. S. 2013, ApJS, 205, 18
Zhang, Q. S. 2016, ApJ, 818, 146
Zhang, Q. S., & Li, Y. 2012a, ApJ, 746, 50
Zhang, Q. S., & Li, Y. 2012b, ApJ, 750, 11